3

LARGE DEFLECTION MODEL: AXIAL STRETCHING EFFECT

3.1 Introduction

In most of the high-speed applications such as turbo-pumps, jet engine etc, the rotor rotates at a significantly high speed, especially at super-critical speed. At such a high speed, a lightweight rotating system can be useful to reduce the critical speed. As the lightweight system is prone to lower stiffness, it consequently leads to a lower critical speed of the system. At high speed, the rotating system often undergoes large deformation under the effect of external disturbance. Major source of nonlinearities in the rotor-bearing system is due to the large deformation. There are many researchers have done work on vibration behavior of rotating systems with geometric nonlinearities due to large deformation of the shaft. A few researches have attempted to analyses on modal characteristics of the rotating system with these nonlinearities by performing the parametric investigation extensively. As well as, the work has been extended to understand the combined effect of nonlinearities with different loading condition on bifurcation and stability of the system.

In a rotating system, a flexible shaft experiences stretching of its axis during the vibration when free movement of the shaft's supports in an axial direction is not allowed. This axial stretching introduces a nonlinear force which in turn affects the overall dynamic behavior of the system. Here, the hinge - hinge type boundary condition for the support of a rotating system is considered. Thus, the axis of the shaft gets stretched. This effect of the axial stretching has been considered in the formulation of the general equation of motion. The evaluation of nonlinear phenomena with a focus on investigating bifurcations and chaotic behavior of a flexible rotating system subjected to an unbalance force, harmonic ground motion and pulsating axial loading has been studied. The bending theory of Euler-Bernoulli has been adopted along with strain displacement relationship with large deformation and the mid-plain stretching phenomenon in the shaft element, a nonlinear mathematical model for the rotating system has been formulated by incorporating the effects of gyroscopic and rotary inertia also. The method of multiple scales is used to obtain the steady state solution of the nonlinear mathematical model and to investigate the overall performance of the system.

3.2 Mathematical formulation: Equation of motion (Phadatare et al., 2017)

In this section, the equation of motion is formulated for a nonlinear rotor-disk system supported by rigid bearings with nonlinearities due to axial stretching and large deflection. The large deflection and the axial stretching of the shaft induce nonlinearities in the system. The rotor system consisting of a flexible shaft with a rigid disk is shown in Fig.3.1.

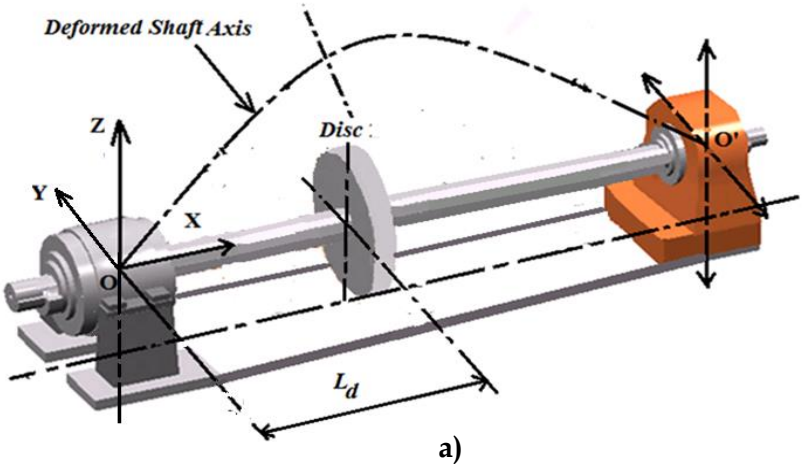

a)

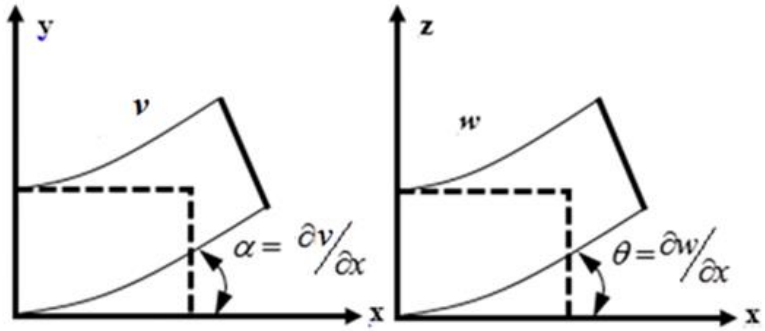

b)

Fig.3.1: a) A rotating system with a rigid bearing **b)** Elastic deformation in transverse direction

a. *Kinetic energy of the flexible shaft and rigid disk*

Considering [Atepor, 2008 and Hosseini, 2009], kinetic energy of the flexible shaft has been determined as an extension of the kinetic energy for an element with length L while the disk mounted on the rotor shaft is assumed to be rigid. The kinetic energy of the flexible shaft can be expressed as (Fig. 3.1)

$$T_s = \frac{1}{2}\int_0^L \left(m(\dot{v}^2 + \dot{w}^2) + I_1\omega_1^2 + I_2(\omega_2^2 + \omega_3^2)\right)dx. \tag{3.1}$$

Kinetic energy of the disk can be expressed as

$$T_d = \frac{1}{2}\int_0^L \left(M_d\{\dot{v}^2 + \dot{w}^2\} + I_{dx}\omega_1^2 + I_{dy}\{\omega_2^2 + \omega_3^2\}\right)\delta(x - L_d)dx. \tag{3.2}$$

Thus, total kinetic energy of the rotating system can be written as

$$\begin{aligned} T_R = T_d + T_s = &\frac{1}{2}\int_0^L \left(\rho A(\dot{v}^2 + \dot{w}^2) + \rho I_1\omega_1^2 + (\rho I_2)(\omega_2^2 + \omega_3^2)\right)dx \\ &+ \frac{1}{2}\int_0^L \left(M\{\dot{v}^2 + \dot{w}^2\} + I_{1d}\omega_1^2 + I_{2d}\{\omega_2^2 + \omega_3^2\}\right)\delta(x - L_d)dx. \end{aligned} \tag{3.3}$$

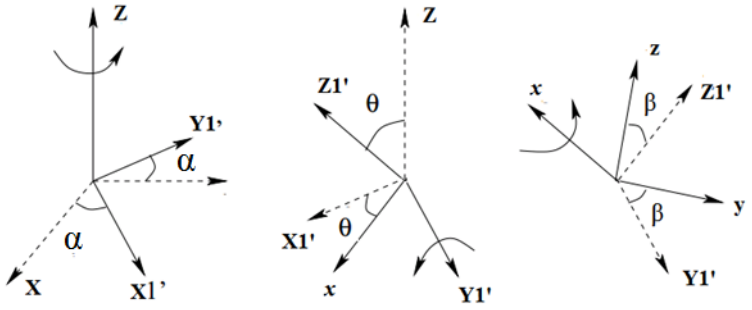

Fig.3.2 : Euler angle rotation

Angular speed of the system can be expressed as following by observing Fig.3.2

$$\omega = \dot{\alpha} e_Z + \dot{\theta} e_{Y1} + \dot{\beta} e_z . \tag{3.4}$$

Here, dot over head of the variables denotes diff. w.r.to time *(t)*. By observing Fig.3.2, the terms in Eq.(3.4) can be written as

$$\begin{aligned} \dot{\alpha} e_Z &= (\cos(\theta) e_{Z1} - \sin(\theta) e_x)\dot{\alpha} \\ &= (\cos(\theta)\left(\cos(\beta) e_z + \sin(\beta) e_y\right) - \sin(\theta) e_x)\dot{\alpha}, \end{aligned} \tag{3.5}$$

$$\dot{\theta} e_{Y1} = \left(\cos(\beta) e_y - \sin(\beta) e_z\right)\dot{\theta}. \tag{3.6}$$

Substituting above Eqs.(3.5)-(3.6) into Eq.(3.4), we get

$$\omega = \omega_1 e_x + \omega_2 e_y + \omega_3 e_z . \tag{3.7}$$

Here,

$$\begin{aligned} \omega_1 &= \dot{\beta} + \dot{\alpha}\sin(\theta); \\ \omega_2 &= \dot{\alpha}\sin(\beta)\cos(\theta) + \dot{\theta}\cos(\beta), \\ \omega_3 &= \dot{\alpha}\cos(\beta)\cos(\theta) - \dot{\theta}\sin(\beta). \end{aligned} \tag{3.8}$$

As the θ becomes small, thus its higher order is neglected, and $\cos(\theta) \approx 1$, $\sin(\theta) \approx \theta$. Substituting Eq. (3.8) into Eq.(3.4), results as

$$\begin{aligned} T_R = &\int_0^L \frac{\rho A}{2}\left(\dot{v}^2 + \dot{w}^2\right) dx + \int_0^L \left(\frac{\rho I}{2}\right)\left(\dot{\alpha}^2 + \dot{\theta}^2\right) dx + \int_0^L (2\rho I)\dot{\alpha}\,\Omega_2\,\theta\, dx \\ &+ \left(\frac{1}{2}\right)(M_d)\int_0^L \left\{\dot{v}^2 + \dot{w}^2\right\}\delta(x - L_d)\, dx + \left(\frac{1}{2}\right)\int_0^l \left\{I_{dy}\left(\dot{\alpha}^2 + \dot{\theta}^2\right) + I_{dx}\dot{\beta}^2 + I_{dx}\dot{\alpha}\,\Omega_2\,\theta\right\}\delta(x - L_d)\, dx . \end{aligned} \tag{3.9}$$

This is an expression of total kinetic energy of the rotor-bearing system. Here, $\dot{\alpha}, \dot{\theta}$ and $\dot{\beta}$ are the time derivatives of the angular displacement about the axes of *Z*, *Y*, and *X*, respectively. Here M_d, ρ, *A*, *I* are the mass of the disk, mass density, cross-sectional area and moment of inertia of the shaft, respectively. Dirac delta function (x-L_d) has been incorporated in order to represent the concentrated disk effect in a distributed system. In this equation, the first three terms represent the kinetic energy of the shaft and the remaining terms corresponding to the kinetic energy of the disk. In this, the third and sixth terms denote consideration of the gyroscopic effect.

b. ***Potential energy stored in flexible shaft element***

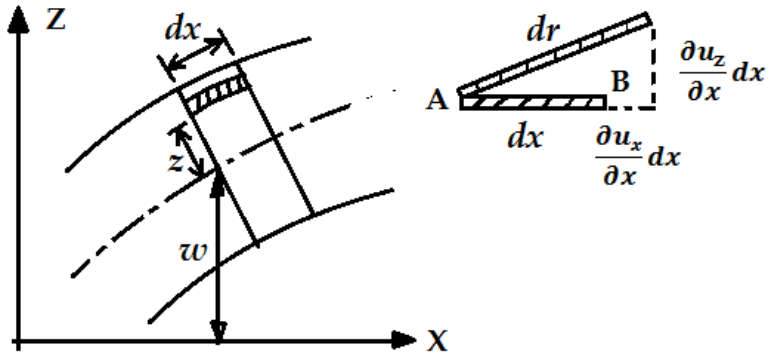

Fig.3.3 : Kinematics of a beam

Deflection along the coordinate axis XYZ are

$$u_x = -z\theta - y\alpha,\ u_y = v,\ u_z = w. \tag{3.10}$$

Point *B* which is at distance *dx* from point A gets shifted by

$$u_{xB} = u_x + \frac{u_x}{x}dx,\quad u_{yB} = u_y + \frac{u_y}{x}dx,\quad u_{zB} = u_z + \frac{u_z}{x}dx. \tag{3.11}$$

Thus, the length of the element *dx* after deformation become

$$dr = \sqrt{\left(dx + \frac{\partial u_x}{\partial x}dx\right)^2 + \left(\frac{\partial u_y}{\partial x}dx\right)^2 + \left(\frac{\partial u_z}{\partial x}dx\right)^2}. \tag{3.12}$$

Where, $\partial u_x/\partial x \ll \partial u_y/\partial x \approx \partial u_z/\partial x$and $\sqrt{1+\beta} = 1 + \beta/2$. Thus, above equation can be expressed as

$$dr \approx dx\left[1 + \frac{\partial u_x}{\partial x} + \frac{1}{2}\left(\frac{\partial u_y}{\partial x}\right)^2 + \frac{1}{2}\left(\frac{\partial u_z}{\partial x}\right)^2\right]. \tag{3.13}$$

$$\varepsilon_x = \frac{dr - dx}{dx} = \left[\frac{\partial u_x}{\partial x} + \frac{1}{2}\left(\frac{\partial u_y}{\partial x}\right)^2 + \frac{1}{2}\left(\frac{\partial u_z}{\partial x}\right)^2\right]. \tag{3.14}$$

We know the values of α and θ from Fig.3.1. Thus, the longitudinal strain (deformation) in the *x* direction is given as (Shad, 2011)

$$\varepsilon_{xx} = -z\frac{\partial\theta}{\partial x} - y\frac{\partial\alpha}{\partial x} \underbrace{+\ \frac{1}{2}\theta^2 + \frac{1}{2}\alpha^2}_{Contribution\ of\ Nonlinear\ part}. \tag{3.15}$$

In Eq.(3.15), first two terms denotes linear strain-displacement relationship and the other terms denote nonlinear strain-displacement relationships due to consideration of the higher order deformation. The strain energy of the shaft can be given as,

$$U = \frac{1}{2}\int_0^L\int_A (\sigma_{xx}\varepsilon_{xx})dAdx. \tag{3.16}$$

By substituting the relation $\sigma_{xx} = E\varepsilon_{xx}$, the strain energy can be expressed as

$$U = \frac{1}{2}\int_0^L\int_A \left(E\varepsilon_{xx}^2\right)dAdx. \tag{3.17}$$

By using Eq.(3.15), the above equation can be written as

$$U = \frac{E}{2}\int_0^L\int_A \left(-z\frac{\partial\theta}{\partial x} - y\frac{\partial\alpha}{\partial x} + \frac{1}{2}\theta^2 + \frac{1}{2}\alpha^2\right)^2 dAdx. \tag{3.18}$$

By expanding the above, we get

$$U=\frac{E}{2}\int_0^L\iint_A\begin{pmatrix}\left(z\frac{\partial\theta}{\partial x}\right)^2+\left(y\frac{\partial\alpha}{\partial x}\right)^2-2yz\left(\frac{\partial\theta}{\partial x}\right)\left(\frac{\partial\alpha}{\partial x}\right)+\frac{1}{4}\theta^4+\frac{1}{4}\alpha^4+\frac{1}{2}\theta^2\alpha^2\\-2\left(z\frac{\partial\theta}{\partial x}+y\frac{\partial\alpha}{\partial x}\right)\left(\frac{1}{2}\theta^2+\frac{1}{2}\alpha^2\right)\end{pmatrix}dAdx\,. \tag{3.19}$$

The cross-section of the rotor is symmetric; thus the 3rd and 7th terms can be neglected from this equation. Therefore, the equation can be rewritten as

$$U=\frac{E}{2}\int_0^L\iint_A\left(\left(z\frac{\partial\theta}{\partial x}\right)^2+\left(y\frac{\partial\alpha}{\partial x}\right)^2+\frac{1}{4}\theta^4+\frac{1}{4}\alpha^4+\frac{1}{2}\theta^2\alpha^2\right)dAdx\,. \tag{3.20}$$

Also, $I_z=\int z^2dA$, $I_y=\int y^2dA$, $I=I_y=I_z$ (due to symmetry).

Thus, the above equation becomes,

$$U=\frac{EI}{2}\int_0^L\left[\left(\frac{\partial\theta}{\partial x}\right)^2+\left(\frac{\partial\alpha}{\partial x}\right)^2\right]dx+\frac{EA}{2}\int_0^L\left[\frac{1}{4}\theta^4+\frac{1}{4}\alpha^4+\frac{1}{2}\theta^2\alpha^2\right]dx\,. \tag{3.21}$$

The total strain energy of the rotor system can now be expressed as

$$U=\int_0^L\left(\frac{EI}{2}\right)\left\{\left(\frac{\partial}{\partial x}\left(\frac{\partial v}{\partial x}\right)\right)^2+\left(\frac{\partial}{\partial x}\left(\frac{\partial w}{\partial x}\right)\right)^2\right\}dx+\int_0^L\left(\frac{EA}{8}\right)\left\{\left(\frac{\partial v}{\partial x}\right)^4+\left(\frac{\partial w}{\partial x}\right)^4+2\left(\frac{\partial v}{\partial x}\right)^2\left(\frac{\partial w}{\partial x}\right)^2\right\}dx\,. \tag{3.22}$$

Here, *EA* and *EI* are considered as axial rigidity and flexural rigidity, respectively. Hinge-hinge type support at the both shaft ends is considered. As a result, the support condition does not allow the shaft ends to move along the axial direction. Thus, an axial force N_A will be applied on the shaft during its bending. This force contributes in the potential energy of the shaft and it can be expressed as,

$$U_{s2}=\frac{N_A}{2}\int_0^L\left(\left(\frac{\partial v}{\partial x}\right)^2+\left(\frac{\partial w}{\partial x}\right)^2\right)dx\,. \tag{3.23}$$

Where, N_A can be written as,

$$N_A=\frac{EA}{2L}\int_0^L\left(\left(\frac{\partial v}{\partial x}\right)^2+\left(\frac{\partial w}{\partial x}\right)^2\right)dx\,. \tag{3.24}$$

By considering the effect of the axial stretching (Eq. (3.23)). The equation for the strain energy (i.e Eq. (3.22)) can be expressed as follow,

$$U_s=\int_0^L\frac{EI}{2}\left[\left(\frac{\partial}{\partial x}\left(\frac{\partial v}{\partial x}\right)\right)^2+\left(\frac{\partial}{\partial x}\left(\frac{\partial w}{\partial x}\right)\right)^2\right]dx+\int_0^L\frac{EA}{2}\left(\frac{1}{4}\left(\frac{\partial v}{\partial x}\right)^4+\frac{1}{4}\left(\frac{\partial w}{\partial x}\right)^4+\frac{1}{2}\left(\frac{\partial v}{\partial x}\right)^2\left(\frac{\partial w}{\partial x}\right)^2\right)dx$$
$$+\int_0^L\int_0^L\frac{EA}{4L}\left(\left(\frac{\partial v}{\partial x}\right)^2+\left(\frac{\partial w}{\partial x}\right)^2\right)dx\left(\left(\frac{\partial v}{\partial x}\right)^2+\left(\frac{\partial w}{\partial x}\right)^2\right)dx \tag{3.25}$$

c. *Approximate Numerical Model*

A displacement shape function is approximated by employing Rayleigh's method for the continuous system. Displacements in the *y* and *z* directions can be expressed as, $v = V(t)\,\varphi(x)$ and $w = W(t)\,\varphi(x)$,where, *V* and *W*are generalized independent coordinates and $\varphi(x)$is the shape function. First mode shape of the shaft with a constant cross section having the hinge-hinge supports at the both ends can be expressed as

$$\varphi(x)= \quad 2\sqrt{2}\sin(\pi x/L), \tag{3.26}$$

The angular displacements can be approximated as,

$$\begin{aligned}
&\partial v/\partial x = \varphi'(x)V = g(x)V,\\
&\partial w/\partial x = \varphi'(x)W = g(x)W,\\
&\frac{\partial}{\partial x}\left(\frac{\partial v}{\partial x}\right) = \varphi''(x)V = h(x)V,\\
&\frac{\partial}{\partial x}\left(\frac{\partial w}{\partial x}\right) = \varphi''(x)W = h(x)W.
\end{aligned} \tag{3.27}$$

Here, $g(x)=\varphi'(x)$, $h(x)=g'(x)=\varphi''(x)$. The prime indicates the derivative with respect to x. Now, using the above expressions (Eq.(3.27)), the total kinetic energy of the rotating system (Eq.(3.9)) in a precise form can be written as,

$$T = T_R = \frac{1}{2}a_1\left(\dot{V}^2+\dot{W}^2\right) - \Omega_2 a_2 \dot{V}W \,. \tag{3.28}$$

$$\text{Here, } a_1 = M_d\varphi^2(x)\big|_{x=L_d} + I_2\left\{\frac{\partial}{\partial x}\varphi(x)\right\}^2\Big|_{x=L_d} + \rho A\int_0^L \varphi^2(x)dx + \rho I_A\int_0^L \varphi^2(x)dx,$$

$$a_2 = \left(I_d\left\{\frac{\partial}{\partial x}\varphi(x)\right\}^2_{x=L_d} + 2\rho I_A\int_0^l\left\{\frac{\partial}{\partial x}\varphi(x)\right\}^2 dx\right).$$

The total strain energy of the rotor system (Eq. (3.25)) can be expressed as,

$$U = \frac{F_1}{2}\left(V^2+W^2\right) + \frac{F_2}{8}\left(V^2+W^2\right)^2 + \frac{F_3}{4}\left(V^2+W^2\right)^2. \tag{3.29}$$

Here,

$$F_1 = EI\int_0^L\left\{\frac{\partial^2}{\partial x^2}\varphi(x)\right\}^2 dx \quad F_2 = EA\left(\int_0^L\left\{\frac{\partial}{\partial x}\varphi(x)\right\}^4 dx\right), \quad F_3 = \frac{EA}{L}\int_0^L\left(\int_0^L\left\{\frac{\partial}{\partial x}\varphi(x)\right\}^4 dx\right)dx.$$

d. *Hamilton's Principle: Derivation of Equations of Motion*

The Hamilton principle is applied on the kinetic and strain energies of the rotating system which is given by equations (3.28) and (3.29) in the form

$$\int_{t_1}^{t_2}\delta(T-U)dt = 0 \,. \tag{3.30}$$

Therefore,

$$\int_{t_1}^{t_2}\delta(T-U\ )dt = \int_{t_1}^{t_2}\delta T dt - \int_{t_1}^{t_2}\delta U dt = 0 \,. \tag{3.31}$$

The two terms in the right-hand side of above equation are treated separately, the first term gives,

$$\int_{t_1}^{t_2}\delta T dt = \int_{t_1}^{t_2}\left[\frac{\partial T_R}{\partial W}\delta W + \frac{\partial T_R}{\partial \dot{V}}\delta\dot{V} + \frac{\partial T_R}{\partial \dot{W}}\delta\dot{W}\right]dt \,. \tag{3.32}$$

Different terms in the above equations are expanded as below,

$$\int_{t_1}^{t_2}\frac{\partial T}{\partial W}\delta W dt = -\int_{t_1}^{t_2}\left(\Omega_2 a_2\dot{V}\delta W\right)dt \,. \tag{3.33}$$

$$\int_{t_1}^{t_2}\frac{\partial T}{\partial \dot{V}}\delta\dot{V}dt = \left[\frac{\partial T}{\partial \dot{V}}\delta\dot{V}\right]_{t_1}^{t_2} - \int_{t_1}^{t_2}\frac{\partial}{\partial t}\left(\frac{\partial T}{\partial \dot{U}}\right)\delta V dt$$

$$= \left[\frac{\partial T_R}{\partial \dot{V}}\delta V\right]_{t_1}^{t_2} - \int_{t_1}^{t_2}\frac{\partial}{\partial t}\left(a_1\dot{V} - \Omega_2 a_2 W\right)\delta V dt \tag{3.34}$$

$$\int_{t_1}^{t_2}\frac{\partial T}{\partial \dot{W}}\delta\dot{W}dt = \left[\frac{\partial T}{\partial \dot{W}}\delta W\right]_{t_1}^{t_2} - \int_{t_1}^{t_2}\frac{\partial}{\partial t}\left(\frac{\partial T}{\partial \dot{W}}\right)\delta W dt \tag{3.35}$$

The second term in the above equation gives,

$$\int_{t_1}^{t_2}\delta U\ dt=\int_{t_1}^{t_2}\left[\frac{\partial U}{\partial V}\delta V+\frac{\partial U}{\partial W}\delta W\right]dt\ . \tag{3.36}$$

The two terms on the right side of the above equation give,

$$\int_{t_1}^{t_2}\frac{\partial U}{\partial V}\delta V dt=\int_{t_1}^{t_2}\left[F_1V+(\frac{1}{2}F_2+F_3)\left(V^3+VW^2\right)^3\right]\delta V dt\ . \tag{3.37}$$

$$\int_{t_1}^{t_2}\frac{\partial U}{\partial W}\delta W dt=\int_{t_1}^{t_2}\left[F_1W+(\frac{1}{2}F_2+F_3)\left(W^3+WV^2\right)\right]\delta W dt\ . \tag{3.38}$$

By collecting the terms of type $\delta V dt$ and $\delta W dt$ from Eqs.(3.33)-(3.38) separately, then following equations can be obtained,

$$-\int_{t_1}^{t_2}\left[\left(\frac{\partial}{\partial t}\left(a_1\dot{V}-\Omega_2a_2W\right)\right)+F_1V+(\frac{1}{2}F_2+F_3)\left(V^3+VW^2\right)\right]\delta V dt=0\ . \tag{3.39}$$

$$-\int_{t_1}^{t_2}\left[\left(\frac{\partial}{\partial t}\left(a_1\dot{W}\right)\right)+\Omega_2a_2\dot{V}+F_1W+(\frac{1}{2}F_2+F_3)\left(W^3+WV^2\right)\right]\delta W dt=0\ . \tag{3.40}$$

By simplifying and re-arranging the above equations (Eqs. (3.39)-(3.40))), it results in

$$a_1\ddot{V}-\Omega_2a_2\dot{W}+F_1V+(\frac{1}{2}F_2+F_3)\left(V^3+VW^2\right)=0\ . \tag{3.41}$$

$$a_1\ddot{W}+\Omega_2a_2\dot{V}+F_1W+(\frac{1}{2}F_2+F_3)\left(W^3+WV^2\right)=0\ . \tag{3.42}$$

These can be further written as,

$$\ddot{V}-\Omega_2\vartheta_1\dot{W}+\vartheta_2V+(\frac{1}{2}\mu_1+\mu_2)\left\{V^3+VW^2\right\}=0. \tag{3.43}$$

$$\ddot{W}+\Omega_2\vartheta_1\dot{V}+\vartheta_2W+(\frac{1}{2}\mu_1+\mu_2)\left\{W^3+WV^2\right\}=0. \tag{3.44}$$

Here$\vartheta_1=a_2/a_1,\ \vartheta_2=F_1/a_1,\ \mu_1=F_2/a_1,\ \mu_2=F_3/a_1$. It has been observed that the equations of motion consist of terms (i.e. $\Omega_2\vartheta_1\dot{W}$ & $\Omega_2\vartheta_1\dot{V}$) due to gyroscopic effect, nonlinear coupled terms (i.e., V^3+VW^2 & W^3+WV^2) due to geometric nonlinearity of the shaft.

e. *Considering a flexible bearing support* (Atepor,2008)

The mathematical expressions are derived for the rotating system by considering the flexible bearings as a support at the ends of the shaft. The bearings are modeled as an equivalent spring-damper system having linear and nonlinear stiffness elements as shown following Fig.3.4.

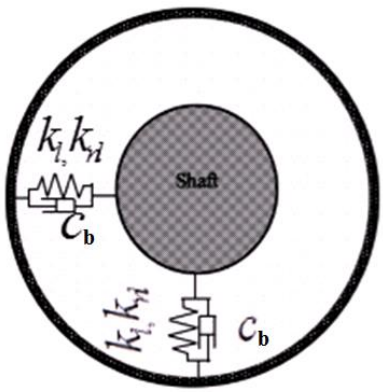

Fig.3.4: Conceptual spring-damper equivalent model for the bearings

The strain energy stored in the bearings can be expressed as

$$U_b = \frac{1}{2}\int_0^L \left[(K_l v + K_{nl} v^3)v + (K_l w + K_{nl} w^3)w\right]\Big|_{x=0} dx$$
$$+ \frac{1}{2}\int_0^L \left[(K_l v + K_{nl} v^3)v + (K_l w + K_{nl} w^3)w\right]\Big|_{x=L} dx \quad (3.45)$$

The total strain energy of the rotating system (Eq. (3.29)) can be expressed as,

$$U = \frac{F_1}{2}\left(V^2 + W^2\right) + \frac{F_2}{8}\left(V^2 + W^2\right)^2 + \frac{F_3}{4}\left(V^2 + W^2\right)^2 + \frac{F_6}{2}\left(V^4 + W^4\right) \quad (3.46)$$

Where,

$$F_1 = EI\int_0^L \left\{\frac{\partial^2}{\partial x^2}\varphi(x)\right\}^2 dx + K_l\int_0^L (\varphi_{x=0}^2 + \varphi_{x=L}^2)dx, \quad F_6 = K_{nl}\int_0^L (\varphi_{x=0}^4 + \varphi_{x=L}^4)dx. \quad (3.47)$$

Where, K_l and K_{nl} are linear and nonlinear bearing coefficients of the bearings respectively. Dirac delta function has been incorporated to represent the bearing effect in the distributed system.

The displacements in the y and z directions can be expressed as, $v = V(t)\,\varphi(x)$ and $w = W(t)\,\varphi(x)$, where, V and W are generalized independent coordinates and $\varphi(x)$ is the trial function, and it has been considered as the normalized 1st mode shape of the shaft with the bearing support and it is given as

$$\varphi(x) = \frac{\left\{\lambda^3 EI\cos(\lambda L) - \lambda^3 EI\cosh(\lambda L) + 2K_l\sinh(\lambda L)\right\}\left(\sin(\lambda x) + \sinh(\lambda x)\right) + \lambda^3 EI\left\{\sinh(\lambda L) - \sin(\lambda L)\right\}\left(\cos(\lambda x) + \cosh(\lambda x)\right)}{\lambda^3 EI\cos(\lambda L) - \lambda^3 EI\cosh(\lambda L) + 2K_l\sin(\lambda L)}. \quad (3.48)$$

This satisfies boundary conditions as

At $x = 0$, $\quad v'' = 0, \quad EIv''' = -(K_l V_0 + c_b\dot{V}_0),\ w'' = 0, \quad EIw''' = -(K_l W_0 + c_b\dot{W}_0)$

At $x = L$, $\quad v'' = 0, \quad EIv''' = (K_l V_l + c_b\dot{V}_l),\ w'' = 0, \quad EIw''' = (K_l W_l + c_b\dot{W}_l).$

Here, the first mode of the vibration has been considered for further analysis since this mode of the vibration is found to be dominant one. The equations of motion of the system (i.e. Eqs (3.43)-(3.44)) can be modified to include the effect of the bearings as expressed below.

$$\ddot{V} - \Omega_2\vartheta_1\dot{W} + \vartheta_2 V + \left(\frac{\mu_1}{2} + \mu_2\right)\left\{V^3 + VW^2\right\} + \vartheta_4 V^3 + c\dot{V} = 0, \quad (3.49)$$

$$\ddot{W} + \Omega_2\vartheta_1\dot{V} + \vartheta_2 W + \left(\frac{\mu_1}{2} + \mu_2\right)\left\{W^3 + WV^2\right\} + \vartheta_4 W^3 + c\dot{W} = 0. \quad (3.50)$$

Where, $\vartheta_4 = 2F_6 / a_1$ and c is a viscous damping of the system. It is observed from the above equations that the terms $\vartheta_4 V^3$ / $\vartheta_4 W^3$ denote nonlinear effect of the bearing.

f. *Excitation of an unbalance mass*

Error in a mechanical system is introduced either at the designing level or manufacturing level or assembly level or during a long-running of the system. One of the major errors in a rotating system is an unbalance which produces a harmonic load on the system during the running condition. The unbalance presence in the system may be due to an error in manufacturing/wear due to long run or improper assembly of rotating parts or extra added mass due to welding or the bolting

In this section, mathematical expressions are formulated to investigate the shaft-disk system under influence of an excitation due to an unbalance mass.

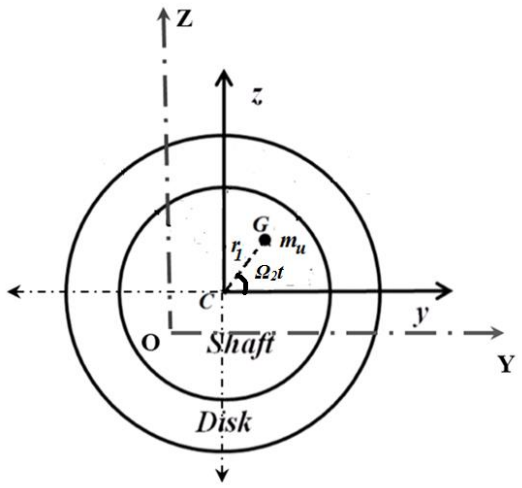

Fig. 3.5: Unbalance mass position

The unbalance mass has been positioned at distance r_1 from the geometric center of the shaft.

Thus

$$OG = \begin{vmatrix} v + r_1 \cos\Omega_2 t \\ w + r_1 \sin\Omega_2 t \end{vmatrix} \tag{3.51}$$

Differentiation OG w.r.to time to get velocity as

$$\frac{\partial(OG)}{\partial t} = \begin{vmatrix} \dot{v} - r_1\Omega_2 \sin(\Omega_2 t) \\ \dot{w} + r_1\Omega_2 \cos(\Omega_2 t) \end{vmatrix} \tag{3.52}$$

We know that the expression for the kinetic energy is

$$T_u = \frac{1}{2} m_u \{(OG)/t)\}^2$$

$$= \frac{1}{2} m_u (\dot{v}^2 + \dot{w}^2 - 2r_1\Omega_2 \dot{w}\sin(\Omega_2 t) + 2r_1\Omega_2 \dot{v}\cos(\Omega_2 t) + r_1{}^2\Omega_2{}^2) \tag{3.53}$$

The effect of mass of the unbalance in the kinetic energy of transverse direction is small compared to mass of the rotor. So, it can be neglected. Thus, the kinetic energy due to the unbalance has been expressed as [Apter, 2008; Rizwan, 2011 and Hosseini, 2009].

$$T_u = m_u \Omega_2 r_1 \left(\dot{v}\cos\Omega_2 t - \dot{w}\sin\Omega_2 t\right) + \frac{m_u}{2}\Omega_2 r_1{}^2. \tag{3.54}$$

Here, m_u, r_1 denote the unbalance mass and an eccentricity of the unbalance with respect to the geometric center of the shaft during operational conditions. The equation of motion of the system i.e. Eqs.(3.43)-(3.44) can be modified to include the effect of the unbalance mass. After some manipulation, it can be represented as

$$\ddot{V} - \Omega_2\vartheta_1\dot{W} + \vartheta_2 V + \left(\frac{1}{2}\mu_1 + \mu_2\right)\left(V^3 + VW^2\right) + c\dot{W} = m_u\Omega_2{}^2 r_1\varphi\left(L_d\right)\cos\Omega_2 t\,. \tag{3.55}$$

$$\ddot{W} + \Omega_2\vartheta_1\dot{V} + \vartheta_2 W + \left(\frac{1}{2}\mu_1 + \mu_2\right)\left(W^3 + V^2 W\right) + c\dot{W} = m_u\Omega_2{}^2 r_1\varphi\left(L_d\right)\sin\Omega_2 t. \tag{3.56}$$

It has been observed that the equations of motion comprise linear damping terms (i.e., $\Omega\vartheta_1\dot{W} + c\dot{V} - \Omega\vartheta_1\dot{V} + c\dot{W}$) due to the gyroscopic effect in addition to the linear viscous effect, nonlinear geometric coupled terms (i.e., $V^3 + VW^2/W^3 + WV^2$) due to the mid-plane stretching effect and the large deformation of the shaft, and forcing terms (i.e., $m_u\Omega_2{}^2 r_1\varphi(L_d)\,sin\,\Omega\,t/\,cos\,\Omega\,t$) due to the mass unbalance. The effect of higher order terms has been neglected. Since the governing equation of motion consists the nonlinear terms, the exact solutions are not available as obtaining closed form is somehow difficult. Therefore, the perturbation approach can be used to find an approximate solution which is described in the following section.

Perturbation Techniques: Solvability Conditions

Time Scaling:

Here, the method of multiple scales is used to find the solution of Eqs (3.55) and (3.56). By following the standard procedures in [Nayfeh, 1995], the displacements (V, W) can be represented in terms of different time scales (T_0, T_1) for first order solutions and a book keeping parameter ε as follows:

$$V(t,\varepsilon) = V_0 + \varepsilon V_1 = V_0(T_0,T_1) + \varepsilon V_1(T_0,T_1). \tag{3.57}$$

$$W(t,\varepsilon) = W_0 + \varepsilon W_1 = W_0(T_0,T_1) + \varepsilon W_1(T_0,T_1). \tag{3.58}$$

Here, $T_n=\varepsilon^n t$ are slow time scales, while T_1 is slower than T_0 and ε is a small dimensionless parameter. T_0 represents a fast time scale. It signifies the motions occurring at the spin rates Ω_2 and the natural frequencies ω_n of the rotor system. T_1 represents a slow-time scaling and it signifies the amplitude and phase variation due to damping, nonlinearity, and resonance. The first and second time derivatives are given by

$$\frac{d}{dt} = D_0 + \varepsilon D_1 + O(\varepsilon^2) + \cdots, \qquad \frac{d^2}{dt^2} = D_0^2 + 2\varepsilon D_0 D_1 + O(\varepsilon^2) + \cdots. \tag{3.59}$$

Here, $D_0 = \partial/\partial T_0$ and $D_1 = \partial/\partial T_1$.

Treatment of the coefficients:

The nonlinear, damping and forcing terms in the equations have been scaled such that it has the same level of ε order as $\mu_1=\varepsilon\mu_1$, $\mu_2=\varepsilon\mu_2$ and $m_u=m_u$. However, $\theta_1=\theta_1$ and $\theta_2=\theta_2$.These assumptions in the time scaling consider the damping terms at a same level of the nonlinear forces. It is needed to obtain the nontrivial solution of the equations of motion. By substituting Eqs.(3.57) - (3.59) into Eqs (3.55) and (3.56), we get

$$\begin{aligned}&\left(D_1\epsilon^2 + 2D_0D_1\epsilon + D_0^2\right)(\epsilon V_1 + V_0) - \Omega_2\theta_1\left(D_1\epsilon + D_0\right)(\epsilon W_1 + W_0) + \theta_2(\epsilon V_1 + V_0) + \epsilon c\left(D_1\epsilon + D_0\right)\\ &\times(\epsilon V_1 + V_0) + \epsilon(1/2\mu_1 + \mu_2)\left((\epsilon V_1 + V_0)^3 + (\epsilon V_1 + V_0)(\epsilon W_1 + W_0)^2\right) = \epsilon m_u \Omega_2{}^2 r_1 \phi_d \cos(\Omega_2 t),\end{aligned} \tag{3.60}$$

$$\begin{aligned}&\left(D_1\epsilon^2 + 2D_0D_1\epsilon + D_0^2\right)(\epsilon W_1 + W_0) + \Omega_2\theta_1\left(D_1\epsilon + D_0\right)(\epsilon V_1 + V_0) + \theta_2(\epsilon W_1 + W_0) + \epsilon(1/2\mu_1 + \mu_2)\\ &\times\left((\epsilon V_1 + V_0)^2(\epsilon W_1 + W_0) + (\epsilon W_1 + W_0)^3\right) + \epsilon c\left(D_1\epsilon + D_0\right)(\epsilon W_1 + W_0) = \epsilon m_u \Omega_2{}^2 r_1 \phi \sin(\Omega_2 t).\end{aligned} \tag{3.61}$$

Then, collecting the coefficients of the like powers of ε, so the above equations can be

$$\begin{aligned}&(D_0{}^2V_0 + \Omega_2\theta_1 D_0 W_0 + \theta_2 V_0)\epsilon\\ &+\begin{pmatrix}2D_0D_1V_0 + D_0{}^2V_1 + \Omega_2\theta_1 D_0 W_0 + \Omega_2\theta_1 D_0 W_1 + \theta_2 V_1\\ +(1/2\mu_1 + \mu_2)\left(V_0{}^3 + V_0 W_0{}^2\right) + cV_0 D_0 - m_u\Omega_2{}^2 r_1\phi\cos(\Omega_2 t)\end{pmatrix}\epsilon + O(\epsilon^2) = 0\end{aligned} \tag{3.62}$$

$$\begin{aligned}&(D_0{}^2W_0 - \Omega_2\theta_1 D_0 V_0 + \theta_2 W_0)\\ &+\begin{pmatrix}2D_0D_1W_0 + D_0{}^2W_1 - \Omega_2\theta_1 D_0 V_0 - \Omega_2\theta_1 V_1 D_0 + \theta_2 W_1\\ +(1/2\mu_1 + \mu_2)\left(V_0{}^2W_0 + W_0{}^3\right) + cD_0 W_0 - m_u\Omega_2{}^2 r_1\phi\sin(\Omega_2 t)\end{pmatrix}\epsilon + \mathcal{O}(\epsilon^2) = 0.\end{aligned} \tag{3.63}$$

Then, we can express the above equations as

System of order *0* equations (ε^0):

$$D_0^2V_0 + \vartheta_2 V_0 + \Omega_2\vartheta_1 D_0 W_0 = 0 \tag{3.64}$$

$$D_0^2W_0 + \vartheta_2 W_0 - \Omega_2\vartheta_1 D_0 V_0 = 0. \tag{3.65}$$

System of order 1 equations (ε^1):

$$\begin{aligned}D_0^2V_1 + \vartheta_2 V_1 + \Omega_2\vartheta_1 D_0 W_1 = &-\Omega_2\vartheta_1 D_0 W_0 - 2D_1D_0V_0 - \frac{\mu_1}{2}V_0^3 - \frac{\mu_1}{2}V_0W_0^2 - \mu_2 V_0^3 - \mu_2 V_0 W_0^2\\ &-\mathrm{c}D_0V_0 + m_u\Omega_2{}^2 r_1\varphi(L_d)\cos\Omega_2 t,\end{aligned} \tag{3.66}$$

$$D_0^2 W_1 + \vartheta_2 W_1 - \Omega_2 \vartheta_1 D_0 V_1 = \Omega_2 \vartheta_1 D_0 V_0 - 2D_1 D_0 W_0 - \frac{\mu_1}{2} W_0^3 - \frac{\mu_1}{2} V_0 W_0^2 - \mu_2 W_0^3 - \mu_2 W_0 V_0^2$$
$$\text{-cD}_0 W_0 + m_u \Omega_2{}^2 r_1 \varphi(L_d) \sin \Omega_2 t \ . \tag{3.67}$$

Secular terms:

The general solution of Eqs (3.64)and (3.65) can be written as,

$$V_0 = D_1(T_1)\exp(i\omega_1 t) + D_2(T_1)\exp(i\omega_2 t) + cc \tag{3.68}$$

$$W_0 = iD_1(T_1)\exp(i\omega_1 t) - iD_2(T_1)\exp(i\omega_2 t) + cc. \tag{3.69}$$

Here, ω_1 and ω_2 are backward and forward natural frequencies of the system and *cc* represents the complex conjugate. By substituting Eqs.(3.68)-(3.69) into Eqs.(3.66)-(3.67) lead to the following two equations

$$\begin{aligned}
&\frac{\partial^2 V_1}{\partial T_0^2} + \partial_2 V_1 + \Omega_2 \vartheta_1 \frac{\partial W_1}{\partial T_0} = \\
&\left[-2i\omega_1 \frac{\partial D_1}{\partial T_1} + \partial_1 \Omega_2 \omega_1 D_1 - ic\omega_1 D_1 - 2\mu_1 D_1^2 \bar{D}_1 - 4\mu_2 D_1^2 \bar{D}_1 - 4\mu_1 D_1 D_2 \bar{D}_2 - 8\mu_2 D_1 D_2 \bar{D}_2\right]\exp(i\omega_1 T_0) - \\
&\left[-2i\omega_2 \frac{\partial D_2}{\partial T_1} - \vartheta_1 \Omega_2 \omega_2 D_2 - ic\omega_2 D_2 - 2\mu_1 D_2^2 \bar{D}_2 - 4\mu_2 D_2^2 \bar{D}_2 - 4\mu_1 D_1 \bar{D}_1 D_2 - 8\mu_2 D_1 \bar{D}_1 D_2\right]\exp(i\omega_2 T_0) - \\
&\left[-\left(2\mu_1 D_2^2 + 4\mu_2 D_2^2\right)\exp i(\omega_1 + 2\omega_2)T_0\right] - \left[\left(2\mu_1 D_1^2 D_2 + 4\mu_2 D_1^2 D_2\right)\exp i(2\omega_1 + \omega_2)T_0\right] \\
&+ \frac{1}{2} m_1 \Omega_2{}^2 u_1 \varphi(L_d)[\exp(i\Omega_2 T_0) + \exp(-i\Omega_2 T_0)] + [cc].
\end{aligned} \tag{3.70}$$

$$\begin{aligned}
&\frac{\partial^2 W_1}{\partial T_0^2} + \vartheta_2 W_1 - \Omega_2 \vartheta_1 \frac{\partial V_1}{\partial T_0} = \\
&\left[2\omega_1 \frac{\partial D_1}{\partial T_1} - i\vartheta_1 \Omega_2 \omega_1 D_1 + c\omega_1 D_1 - 2i\mu_1 D_1^2 D_1 - 4i\mu_2 D_1^2 \bar{D}_1 - 4i\mu_1 D_1 D_2 \bar{D}_2 - 8i\mu_2 D_1 D_2 \bar{D}_2\right]\exp(i\omega_1 T_0) - \\
&\left[2\omega_2 \frac{\partial D_1}{\partial T_1} + i\vartheta_1 \Omega_2 \omega_2 D_2 + c\omega_2 D_2 - 2i\mu_1 D_2^2 \bar{D}_2 - 4i\mu_2 D_2^2 \bar{D}_2 - 4i\mu_1 D_1 \bar{D}_1 D_2 - 8i\mu_2 D_1 \bar{D}_1 D_2\right]\exp(i\omega_2 T_0) \\
&+ \left[\left(2i\mu_1 D_1 D_2^2 + 4i\mu_2 D_1 D_2^2\right)\text{expi}(\omega_1 + 2\omega_2)T_0\right] - \left[\left(2i\mu_1 D_1^2 D_2 + 4i\mu_2 D_2\right)\exp i(2\omega_1 + \omega_2)T_0\right] + \\
&- \frac{1}{2} i m_1 \Omega_2{}^2 u_1 \varphi_d[\exp(i\Omega_2 T_0) - \exp(-i\Omega_2 T_0)] + [cc].
\end{aligned} \tag{3.71}$$

Here, the *cc* stands for the complex conjugate. Even, the response of the system is bounded but the solutions of the system at some conditions will not be bounded due to the existence of the secular terms in Eqs.(3.70) -(3.71).

Solvability condition:

To get condition of solvability, we assume a particular solution of V_1 and W_1 in the form,

$$V_1 = P_1(T_1)\exp(i\omega_1 t) + Q_1(T_1)\exp(i\omega_2 t) + cc \tag{3.72}$$

$$W_1 = P_2(T_1)\exp(i\omega_1 t) + Q_2(T_1)\exp(i\omega_2 t) + cc. \tag{3.73}$$

Substituting these equations to the left side of Eqs.(3.70) -(3.71), Then the coefficient of $e^{i\omega_1 t}$ of the resulting equations (LHS) are

$$R_{11} = i\Omega_2 \theta_1 P_2 \omega_1 - P_1 \omega_1{}^2 + \theta_2 P_1, \tag{3.74}$$

$$R_{12} = -i\Omega_2 \theta_1 P_1 \omega_1 - P_2 \omega_1{}^2 + \theta_2 P_2. \tag{3.75}$$

Then the coefficient of $e^{i\omega_2 t}$of the resulting equations (LHS) are

$$S_{11} = i\Omega_2 \theta_1 Q_2 \omega_2 - Q_1 \omega_2^{\,2} + \theta_2 Q_1 \tag{3.76}$$

$$S_{12} = -i\Omega_2 \theta_1 Q_1 \omega_2 - Q_2 \omega_{\partial}^{\,2} + \theta_2 Q_2 . \tag{3.77}$$

It may be noted that Eqs.(3.70) -(3.71) has secular or small divisor terms when the system is subjected to following resonance conditions.
$(i).\ \Omega_2 = \omega_1$, (ii). $\Omega_2 = \omega_2$. In the following subsections, the resonance conditions are observed when the frequency of the unbalance is nearly equal to the backward and forward natural frequency of the system $i.e., \Omega_2 = \omega_1$, and $\Omega_2 = \omega_2$.

i) Case of $\Omega_2 \approx \omega_1$

Substituting $\Omega_2 = \omega_1 + \varepsilon\sigma_1$,(where σ_1 is a detuning parameter for controlling the nearness of Ω_2 to ω_1) into Eqs.(3.70) -(3.71), we get

$$\left[\begin{array}{l} -2i\omega_1 \dfrac{\partial D_1}{\partial T_1} + \partial_1 \Omega_2 \omega_1 D_1 - ic\omega_1 D_1 - 2\mu_1 D_1^2 \bar{D}_1 - 4\mu_2 D_1^2 \bar{D}_1 - 4\mu_1 D_1 D_2 \bar{D}_2 - 8\mu_2 D_1 D_2 \bar{D}_2 \\ + \dfrac{1}{2} m_1 \Omega_2^{\,2} r_1 \varphi_d \exp(i\varepsilon\sigma_1 T_0) \end{array}\right] \exp(i\omega_1 T_0) -$$

$$\left[-2i\omega_2 \frac{\partial D_2}{\partial T_1} - \vartheta_1 \Omega_2 \omega_2 D_2 + ic\omega_2 D_2 - 2\mu_1 D_2^2 \bar{D}_2 - 4\mu_2 D_2^2 \bar{D}_2 - 4\mu_1 D_1 \bar{D}_1 D_2 - 8\mu_2 D_1 \bar{D}_1 D_2\right] \exp(i\omega_2 T_0)$$

$$\left[-\left(2\mu_1 D_2^2 + 4\mu_2 D_2^2\right) \exp i(\omega_1 + 2\omega_2) T_0\right] - \left[\left(2\mu_1 D_1^2 D_2 + 4\mu_2 D_1^2 D_2\right) \exp i(2\omega_1 + \omega_2) T_0\right] + [cc]. \tag{3.78}$$

$$\frac{\partial^2 W_1}{\partial T_0^2} + \vartheta_2 W_1 + \Omega_2 \vartheta_1 \frac{\partial V_1}{\partial T_0} =$$

$$\left[\begin{array}{l} 2\omega_1 \dfrac{\partial D_1}{\partial T_1} - i\vartheta_1 \Omega_2 \omega_1 D_1 + c\omega_1 D_1 - 2i\mu_1 D_1^2 D_1 - 4i\mu_2 D_1^2 \bar{D}_1 - 4i\mu_1 D_1 D_2 \bar{D}_2 \\ - 8i\mu_2 D_1 D_2 \bar{D}_2 + \dfrac{1}{2} m_1 \Omega_2^{\,2} r_1 \varphi_d \exp(\varepsilon i\sigma_1 T_0) \end{array}\right] \exp(i\omega_1 T_0) -$$

$$\left[2\omega_2 \frac{\partial D_1}{\partial T_1} - i\vartheta_1 \Omega_2 \omega_2 D_2 + c\omega_2 D_2 — 2i(\mu_1 + 2\mu_2) D_2^2 \bar{D}_2 - 4i\mu_1 D_1 \bar{D}_1 D_2 - 8i\mu_2 D_1 \bar{D}_1 D_2\right] \exp(i\omega_2 T_0)$$

$$+\left[\left(2i\mu_1 D_1 D_2^2 + 4i\mu_2 D_1 D_2^2\right) \exp i(\omega_1 + 2\omega_2) T_0\right] - \left[\left(2i\mu_1 D_1^2 D_2 + 4i\mu_2 D_2\right) \exp i(2\omega_1 + \omega_2) T_0\right] + [cc]. \tag{3.79}$$

So the secular terms related to $e^{i\omega_1 t}$on the right side of the Eqs.(3.78)-(3.79) are

$$R_{21} = -2i\omega_1 \frac{\partial D_1}{\partial T_1} + \partial_1 \Omega_2 \omega_1 D_1 - ic\omega_1 D_1 - 2\mu_1 D_1^2 \bar{D}_1 - 4\mu_2 D_1^2 \bar{D}_1 - 4\mu_1 D_1 D_2 \bar{D}_2 - 8\mu_2 D_1 D_2 \bar{D}_2$$

$$+ \frac{1}{2} m_1 \Omega_2^{\,2} r_1 \varphi_d \exp(\varepsilon i\sigma_1 T_0) . \tag{3.80}$$

$$R_{22} = 2\omega_1 \frac{\partial D_1}{\partial T_1} - i\vartheta_1 \Omega_2 \omega_1 D_1 + c\omega_1 D_1 - 2i\mu_1 D_1^2 D_1 - 4i\mu_2 D_1^2 \bar{D}_1 - 4i\mu_1 D_1 D_2 \bar{D}_2 - 8i\mu_2 D_1 D_2 \bar{D}_2$$

$$- \frac{1}{2} i m_1 \Omega_2^{\,2} r_1 \varphi_d \exp(\varepsilon i\sigma_1 T_0), \tag{3.81}$$

So the secular terms are related to $e^{i\omega_2 t}$ on the right side of the Eqs.(3.78)-(3.79) are

$$S_{21} = -2i\omega_2 \frac{\partial D_2}{\partial T_1} - \vartheta_1 \Omega_2 \omega_2 D_2 + ic\omega_2 D_2 - 2\mu_1 D_2^2 \bar{D}_2 - 4\mu_2 D_2^2 \bar{D}_2 - 4\mu_1 D_1 \bar{D}_1 D_2 - 8\mu_2 D_1 \bar{D}_1 D_2 \tag{3.82}$$

$$S_{22} = -2\omega_2 \frac{\partial D_2}{\partial T_1} - i\vartheta_1 \Omega_2 \omega_2 D_1 + c\omega_2 D_2 + 2i\mu_1 D_2^2 \bar{D}_2 + 4i\mu_2 D_2^2 \bar{D}_2 + 4i\mu_1 D_1 \bar{D}_1 D_2 + 8i\mu_2 D_1 \bar{D}_1 D_2$$

$$+\left[\left(2i\mu_1 D_1 D_2^2 + 4i\mu_2 D_1 D_2^2\right) \exp i(\omega_1 + 2\omega_2) T_0\right] - \left[\left(2i\mu_1 D_1^2 D_2 + 4i\mu_2 D_2\right) \exp i(2\omega_1 + \omega_2) T_0\right] + [cc]. \tag{3.83}$$

Thus, solvability conditions can be written using Eqs. (3.74)-(3.77) and Eqs.(3.80)-(3.83) as (Hosseini et al, 2005)

$$\begin{pmatrix} -\omega_1^2+\theta_2 & i\Omega_2\theta_1\omega_1 \\ R_{21} & R_{22} \end{pmatrix}=0,\ \begin{pmatrix} -\omega_2^2+\theta_2 & i\Omega_2\theta_1\omega_2 \\ S_{21} & S_{22} \end{pmatrix}=0. \tag{3.84}$$

By solving the above equations, the solvability equations can be

$$-2\omega_1\frac{\partial D_1}{\partial T_1}-i\Omega_2\theta_1\omega_1 D_1-c\omega_1 D_1+2i(\mu_1+2\mu_2)D_1^2\overline{D_1}+4i(\mu_1+2\mu_2)D_1D_2\overline{D_2} \tag{3.85}$$
$$+(i/2)\Omega_2^2\phi m_u r_1 e^{iT_1\sigma}=0$$

$$-2\omega_2\frac{\partial D_2}{\partial T_1}+i\Omega_2\theta_1\omega_2 D_2-c\omega_2 D_2+2i(\mu_1+2\mu_2)D_2^2\overline{D_2}+4i(\mu_1+2\mu_2)D_1D_2\overline{D_1}=0 \tag{3.86}$$

Modulation of equations

Substituting the solutions of D_1 and D_2 of the polar form i.e., $D_n=(1/2)a_n\,exp(i\varphi_n)$ where n = 1, 2 into Eqs.(3.85)-(3.86), then the real and imaginary parts have been separated. It results into an autonomous system of four first order partial differential equations which have been expressed as

$$\frac{\partial a_2}{\partial T_1}+(c/2)a_2=0,$$

$$\frac{\partial\theta_2}{\partial T_1}(4\omega_2 a_2)-(\mu_1+2\mu_2)a_2^3+2\omega_2 c a_1^2 a_2-2\omega_2\Omega_2\,\vartheta_1 a_2=0,$$

$$\frac{\partial a_1}{\partial T_1}(2\omega_2)+2ca_1+2m_u\Omega_2^2 r_1\varphi(L_d)\sin(\alpha)=0,$$

$$\frac{\partial\alpha}{\partial T_1}(4\omega_1 a_1)-4\omega_1 a_1\sigma_1+(\mu_1+2\mu_2)a_2^3+2(\mu_1+2\mu_2)a_1a_2^2+2\omega_1\Omega_2\vartheta_1 a_1+2m_u\Omega_2^2 r_1\varphi(L_d)\cos(\alpha)=0. \tag{3.87}$$

Here,$\alpha=-\varphi_1+\sigma_1 T_1$. For the steady state and equilibrium solutions, one may set up $q_2^{/}=0$, and $\alpha^{/}=0$. Nontrivial solutions exist and we can use equations $a_1=a_{10}+a_1^{/}$, $a_2=a_{20}+a_2^{/}$ and $\alpha=\alpha_0+\alpha^{/}$ into above equations to find the stability of the steady state responses for the perturbation analysis and then to investigate the eigen-values of the resulting Jacobian matrix (*J*).

ii) Case of $\Omega_2\approx\omega_2$

Adopting similar approach for the case of taking $\Omega_2=\omega_2+\varepsilon\sigma_1$, we obtained the following autonomous system of four first order partial differential equations as follows.

$$\frac{\partial a_2}{\partial T_1}+(c/2)a_2=0,$$

$$\frac{\partial\theta_2}{\partial T_1}(4\omega_1 a_2)-(\mu_1+2\mu_2)a_2^3+2\omega_1 c a_1^2 a_2-2\omega_1\Omega_2\vartheta_1 a_2=0,$$

$$\frac{\partial a_1}{\partial T_1}(2\omega_2)+2ca_1+2m_u\Omega_2^2 r_1\varphi(l_d)\sin(\alpha)=0,$$

$$\frac{\partial\alpha}{\partial T_1}(4\omega_2 a_1)-4\omega_2 a_1\sigma_1+(\mu_1+2\mu_2)a_1^3+2(\mu_1+2\mu_2)a_1a_2^2+2\omega_2\Omega_2\vartheta_1 a_1+2m_u\Omega_2^2 r_1\varphi(l_d)\cos(\alpha)=0. \tag{3.88}$$

Here, $\alpha=-\theta_2+\sigma_1 T_1$. For steady state and equilibrium solutions, one may set up $q_2^{/}=0$, and $\alpha^{/}=0$. Nontrivial solutions exist and the stability of the steady state responses can be obtained by perturbing Eqs. (3.88) with $a_1=a_{10}+a_1^{/}$, $a_2=a_{20}+a_2^{/}$ and $\alpha=\alpha_0+\alpha^{/}$ and then analyzing the eigen-values of the corresponding Jacobian matrix (*J*). This set of autonomous equations is useful to determine the stability and bifurcation of the steady state response of the system near the resonance condition and the characteristics are plotted using the frequency response plots.

3.3 Excitation of a base motion and an unbalance mass

There are unpredictable external excitation/uncertain means which affect the dynamic behavior and proper functioning of the system. One of the excitations is a base motion. In heavy industries, processing machines are installed with a rigid base support, but the vibration of surrounding machines gets transferred to the base of the machine and affects the system overall performance. Earthquake or loose/improper construction of the base is also another source of a base excitation. In automobiles, the rotating parts are always subjected to base motion during riding over bad roads or bumpers.

In this section, an investigation of the stability and bifurcation of a nonlinear rotor-disk system supported by rigid bearings under excitations of base motion and unbalance mass. The mathematical expressions are formulated to analyze the dynamic behavior of a shaft disk system having transverse movement of the support by taking into account the effect of the nonlinearities due to higher order deformation in bending and axial stretching.

3.3.1 Analysis

The rotor system consisting of a flexible shaft, rigid disk and rigid bearings is shown in Fig. 3.6, which subjected to ground motion $Z = Z_a \cos \omega t$.

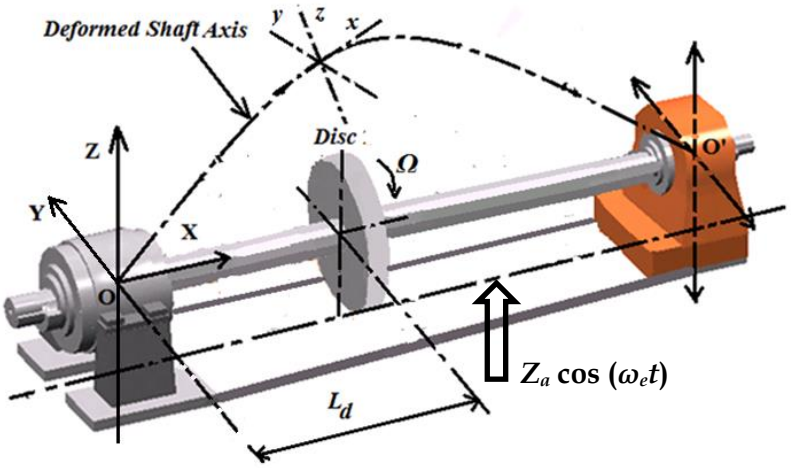

Fig. 3.6: A rotor bearing system under moving platform

The kinetic energy of the rotating system with the base excitation is derived by extending Eq. (3.9). Thus, the expression for the kinetic energy of the rotor-bearing system with the moving platform can be written as.

$$T_t = \int_0^L \frac{\rho A}{2}\left(\dot{v}^2 + \left(\dot{w} + \frac{d}{dt}\langle Z_a \cos\omega_e t\rangle\right)^2\right)dx + \int_0^L \left(\frac{\rho I}{2}\right)\left(\dot{\alpha}^2 + \dot{\theta}^2\right)dx + \int_0^L (2\rho I)\dot{\alpha}\,\Omega_2\,\theta\,dx + \left(\frac{1}{2}\right)(m)$$
$$\int_0^L \left\{\dot{v}^2 + \left(\dot{w} + \frac{d}{dt}\langle Z_a \cos\omega_e t\rangle\right)^2\right\}\delta(x - l_d)dx + \left(\frac{1}{2}\right)\int_0^L \left\{I\dot{\alpha}^2 + I_z\left(\dot{\theta}^2 + \dot{\beta}^2\right)\right\}\delta(x - L_d)dx. \quad (3.89)$$

Here, Z_a, and ω_e are a magnitude and a frequency of the moving platform. The equations of motion of the system (i.e. Eqs (3.43)-(3.44)) can be modified to include effects of the base motion and the unbalance. After some manipulation, it can be represented as

$$\ddot{V} - \Omega_2\vartheta_1\dot{W} + \vartheta_2 V + \left(\frac{1}{2}\mu_1 + \mu_2\right)\left(V^3 + VW^2\right) + c\dot{W} = m_u{\Omega_2}^2\mu_1\varphi(L_d)\cos\Omega_2 t\,, \quad (3.90)$$

$$\ddot{W} + \Omega_2\vartheta_1\dot{V} + \vartheta_2 W + \left(\frac{1}{2}\mu_1 + \mu_2\right)\left(W^3 + V^2W\right) + c\dot{W} = m_u{\Omega_2}^2\mu_1\varphi(L_d)\sin\Omega_2 t + +\gamma Z_a{\omega_e}^2\cos\omega_e t\,. \quad (3.91)$$

The expressions for coefficients (ϑ_1, ϑ_2 and μ_1) have been already expressed in the previous sections and additional coefficient (γ) can be expressed as

$$\gamma = \left(2M_d \varphi^2(x)\Big|_{x=L_d} + 2\rho A \int_0^L \varphi(x)\,dx \right) \Big/ a_1 . \tag{3.92}$$

It has been observed that the equations of motion comprise the nonlinear terms and forcing terms (i.e., $m_u \Omega_2^2 \mu_1 \varphi(L_d)\, sin\, \Omega_2\, t + \gamma Z_a \omega_e{}^2\, cos\, \omega_e\, t$) due to the mass unbalance and the base excitation in transverse direction. Since the governing equations of motion (i.e., Eqs.(3.90)-(3.91)) contain the nonlinear terms, an approximate solution for the system of equation can be sought by using the perturbation approach. A similar treatment of the method of multiple scales as described in the previous section is adopted. Then, it results into following equations for order 1 of ε

$$\begin{aligned}
&\frac{\partial^2 V_1}{\partial T_0^2} + \partial_2 V_1 - \Omega_2 \vartheta_1 \frac{\partial W_1}{\partial T_0} = \\
&\left[-2i\omega_1 \frac{\partial D_1}{\partial T_1} - \partial_1 \Omega_2 \omega_1 D_1 - ic\omega_1 D_1 - 2\mu_1 D_1^2 \bar{D}_1 - 4\mu_2 D_1^2 \bar{D}_1 - 4\mu_1 D_1 D_2 \bar{D}_2 - 8\mu_2 D_1 D_2 \bar{D}_2 \right] \exp(i\omega_1 T_0) - \\
&\left[-2i\omega_2 \frac{\partial D_2}{\partial T_1} + \vartheta_1 \Omega_2 \omega_2 D_2 - ic\omega_2 D_2 - 2\mu_1 D_2^2 \bar{D}_2 - 4\mu_2 D_2^2 \bar{D}_2 - 4\mu_1 D_1 \bar{D}_1 D_2 - 8\mu_2 D_1 \bar{D}_1 D_2 \right] \exp(i\omega_2 T_0) - \\
&\left[-\left(2\mu_1 D_2^2 + 4\mu_2 D_2^2\right) \exp i(\omega_1 + 2\omega_2) T_0 \right] - \left[\left(2\mu_1 D_1^2 D_2 + 4\mu_2 D_1^2 D_2\right) \exp i(2\omega_1 + \omega_2) T_0 \right] \\
&+ \frac{1}{2} m_1 \Omega_2{}^2 u_1 \varphi(L_d) [\exp(i\Omega_2 T_0) + \exp(-i\Omega_2 T_0)] + [cc].
\end{aligned} \tag{3.93}$$

$$\begin{aligned}
&\frac{\partial^2 W_1}{\partial T_0^2} + \vartheta_2 W_1 + \Omega_2 \vartheta_1 \frac{\partial V_1}{\partial T_0} = \\
&\left[2\omega_1 \frac{\partial D_1}{\partial T_1} + \vartheta_1 \Omega_2 \omega_1 D_1 + c\omega_1 D_1 - 2i\mu_1 D_1^2 D_1 - 4i\mu_2 D_1^2 \bar{D}_1 - 4i\mu_1 D_1 D_2 \bar{D}_2 - 8i\mu_2 D_1 D_2 \bar{D}_2 \right] \exp(i\omega_1 T_0) - \\
&\left[2\omega_2 \frac{\partial D_1}{\partial T_1} - i\vartheta_1 \Omega_2 \omega_1 D_2 + c\omega_2 D_2 - 2i\mu_1 D_2^2 \bar{D}_2 - 4i\mu_2 D_2^2 \bar{D}_2 - 4i\mu_1 D_1 \bar{D}_1 D_2 - 8i\mu_2 D_1 \bar{D}_1 D_2 \right] \exp(i\omega_2 T_0) \\
&+ \left[\left(2i\mu_1 D_1 D_2^2 + 4i\mu_2 D_1 D_2^2\right) \exp i(\omega_1 + 2\omega_2) T_0 \right] - \left[\left(2i\mu_1 D_1^2 D_2 + 4i\mu_2 D_2\right) \exp i(2\omega_1 + \omega_2) T_0 \right] + \\
&- \frac{1}{2} i m_1 \Omega_2{}^2 u_1 \varphi_d [\exp(i\Omega_2 T_0) - \exp(-i\Omega_2 T_0)] + \frac{1}{2} \gamma \omega_e^2 B_0 [\exp(i\omega_e T_0) + \exp(-i\Omega_2 T_0)] + [cc].
\end{aligned} \tag{3.94}$$

Eqs.(3.93)-3.13 have secular or small divisor terms when the system is subjected to following resonance conditions.

(i). $\omega_e = \omega_1$, (ii). $\omega_e = \omega_2$,
(iii). $\Omega_2 = \omega_1$, (iv). $\Omega_2 = \omega_2$,
(v). $\omega_e = \Omega_2 = \omega_1$, (vi). $\omega_e = \Omega_2 = \omega_2$.

In order to obtain a bounded solution, the secular or small divisor terms are required to be removed. In the next subsections, the resonance conditions are discussed when frequency of harmonically varying support motion is nearly equal to the backward and forward natural frequency of the system $i.e., \omega_e = \omega_1$, and $\omega_e = \omega_2$.

Resonance condition: $\omega_e \approx \omega_1$

Substituting the solutions of D_1 and D_2in the polar form i.e., $D_n = (1/2) a_n\, exp(i\varphi_n)$ where n = 1, 2 in the resulting equations which is obtained by substituting, $\omega_e = \omega_1 + \varepsilon\sigma_1$, where σ_1 is a detuning parameter for controlling the nearness of ω_e to ω_1 into (3.93) - 3.13. To determine the solvability conditions, equating the coefficients of *exp* ($i\omega_1 T_0$) and *exp*($i\omega_2 T_0$) on both sides of the resultant equations and then separating the real and imaginary parts. It results into an

autonomous system of four first order partial differential equations which have been expressed as

$$\frac{\partial a_1}{\partial T_1}+(c/2)a_1=0,$$
$$\frac{\partial \theta_2}{\partial T_1}(4\omega_2 a_1)-(\mu_1+2\mu_2)a_1^3+2\omega_2 c a_2^2 a_1-2\omega_2\Omega_2\,\vartheta_1 a_1=0,$$
$$\frac{\partial a_2}{\partial T_1}(2\omega_2)+2ca_2+2\gamma\omega_e^2 B_0\cos(\alpha)=0,$$
$$\frac{\partial \alpha}{\partial T_1}(4\omega_1 a_2)-4\omega_1 a_2\sigma_1+(\mu_1+2\mu_2)a_2^3+2(\mu_1+2\mu_2)a_2 a_1^2+2\omega_1\Omega_2\vartheta_1 a_2+2\gamma\omega_e^2 B_0\sin(\alpha)=0. \quad (3.95)$$

Here, $\alpha=-\varphi_1+\sigma_1 T_1$. For the steady state and equilibrium solutions, one may set up $a_1^{/}=0$, and $\alpha^{/}=0$.

Resonance condition: $\omega_e \approx \omega_2$

Adopting the similar approach for the case of taking $\omega_e=\omega_2+\varepsilon\sigma_1$, we obtained the following an autonomous system of four first order partial differential equations.

$$\frac{\partial a_2}{\partial T_1}+(c/2)a_2=0,$$
$$\frac{\partial \theta_2}{\partial T_1}(4\omega_1 a_2)-(\mu_1+2\mu_2)a_2^3+2\omega_1 c a_1^2 a_2-2\omega_1\Omega_2\vartheta_1 a_2=0,$$
$$\frac{\partial a_1}{\partial T_1}(2\omega_2)+2ca_1+2\gamma\omega_e^2 B_0\sin(\alpha)=0,$$
$$\frac{\partial \alpha}{\partial T_1}(4\omega_2 a_1)-4\omega_2 a_1\sigma_1+(\mu_1+2\mu_2)a_1^3+2(\mu_1+2\mu_2)a_1 a_2^2+2\omega_2\Omega_2\vartheta_1 a_1+2\gamma\omega_e^2 B_0\cos(\alpha)=0. \quad (3.96)$$

Here, $\alpha=-\varphi_2+\sigma_1 T_1$. The values of $a_1^{/}$ and $\alpha^{/}$ in above equations have to be neglected to obtain the steady state and equilibrium solutions of the system. Nontrivial solutions exist and to find the stability of the steady state responses, one may perturb Eqs. 3.16 with $a_1=a_{10}+a_1^{/}$, $a_2=a_{20}+a_2^{/}$ and $\alpha=\alpha_0+\alpha^{/}$ and then investigating the eigen-values of the resulting Jacobian matrix (*J*).

Resonance condition: $\omega_e \approx \Omega_2 \approx \omega_1$

The similar procedures as that of adopted in the previous sub-sections have been used for the case of $\omega_e \approx \Omega \approx \omega_1$. A similar autonomous system of four first order partial differential equations has been obtained where α and can be expressed as $-\theta_1+\sigma_1 T_1$ and term $\gamma\omega_e^2 B_0$ can be rewritten as $(\gamma\omega_e^2 B_0+2m_1{\Omega_2}^2\mu_1)$. The zero steady state response amplitude may observe for a_2 and one may set up $a_1^{/}=0$, and $\alpha^{/}=0$ for obtaining the non-trivial solution for a_2 at steady state conditions. Nontrivial solutions exist for above equations and the stability of the steady state responses can be determined by investigating the eigen-values of the Jacobian matrix (*J*).

3.3.2 Results and discussion

In all the simulations, the rotor system has been considered with the shaft length L = 0.5 *m*, shaft radius R_s=*0.01 m,* disk radius R_d=*0.12,* disk position L_d = *L/3*, damping constant c = 0.001 N-s/m and material with Young's modulus E and density ρ equal to 2x 10^{11} N/m^2 and 7800 kg/m^3, respectively. Numerical calculations have been carried out for free and forced vibration analysis with a ground excitation. The forced vibration analysis with the ground motion has been investigated to obtain the frequency response curves under steady-state conditions along with nonlinear attributes accompanied by chaotic behaviors under the changes of design parameters such as the amplitude of the ground motion, the mass of disk, location of disk and radius of the shaft. Thus, Sect. 3.3.2(*a)* shows the influence of geometry and material properties of the shaft on

the forward and backward whirl speeds, while Sect. 3.3.2(*b)* displays the chaotic behaviors, i.e., reveals the route to chaos from the quasi-periodic response. Section 3.3.2(*c*) demonstrates the steady-state responses under variation of the various system variables for the resonance conditions.

a. *Critical Speeds: Campbell diagram*

The forward and backward whirl frequencies of the shaft depend on the rotor geometry and material properties of the shaft. In the present investigation, the material properties have been considered to be the same, and the analysis has been made for changing the rotor geometry. Effects of the various parameters springing up from the geometry of the rotor shaft have been illustrated to find the forward and backward whirl frequencies.

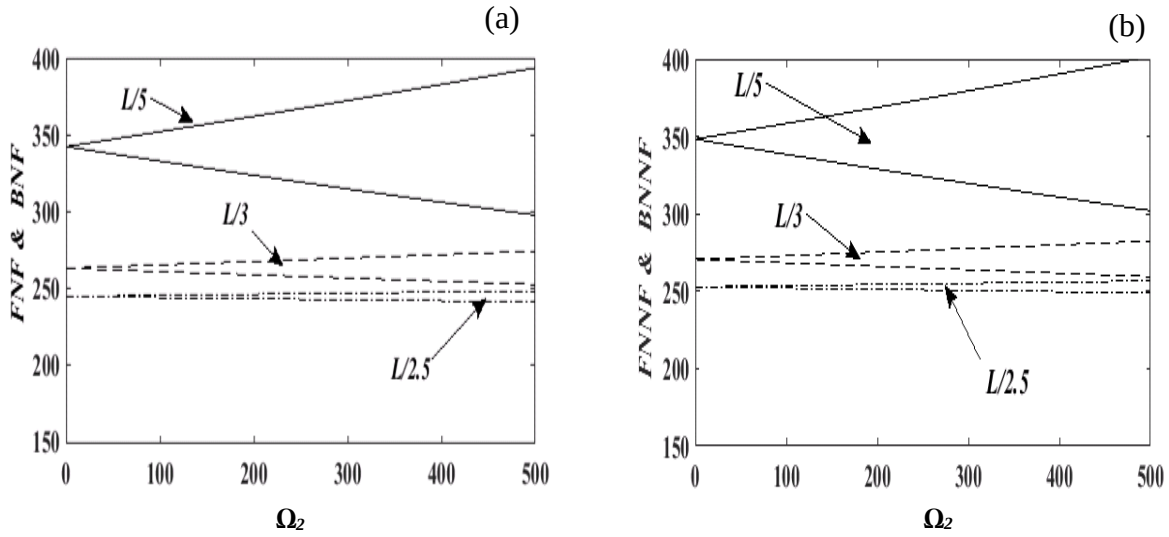

Fig.3.7: Effect of a location of the disk on the both linear and nonlinear forward and backward natural frequencies

Figure 3.7 illustrates the variation of the critical speeds for the different disk positions. It has been clearly observed that the whirling speeds of the rotor are significantly influenced by the location of the disk, while the critical speed decreases with the disk position move away from the bearing end. It is also indicated that the rotor shaft system operates with a single frequency when the location of the disk is at the mid-point of the shaft element since the effect of the gyroscopic couple is neutralized at this location. Hence, the difference between forward and backward speeds increases when the disk position is moving away from the midpoint. The natural frequencies are influenced by the nonlinear terms due to the mid-plane stretching and appeared to be higher value with the presence of the nonlinear coupling terms. However, the behavior patterns are observed to be similar as that of the linear part. This is considered to be crucial because the effective spring constant gets increased with the mid-plane stretching or geometric nonlinearity. Hence, slope, i.e., $\partial N / \partial \Omega_2$ is found to be constant for the both linear and nonlinear frequencies, but an unceasing change in the natural frequencies has been observed for the nonlinear effect.

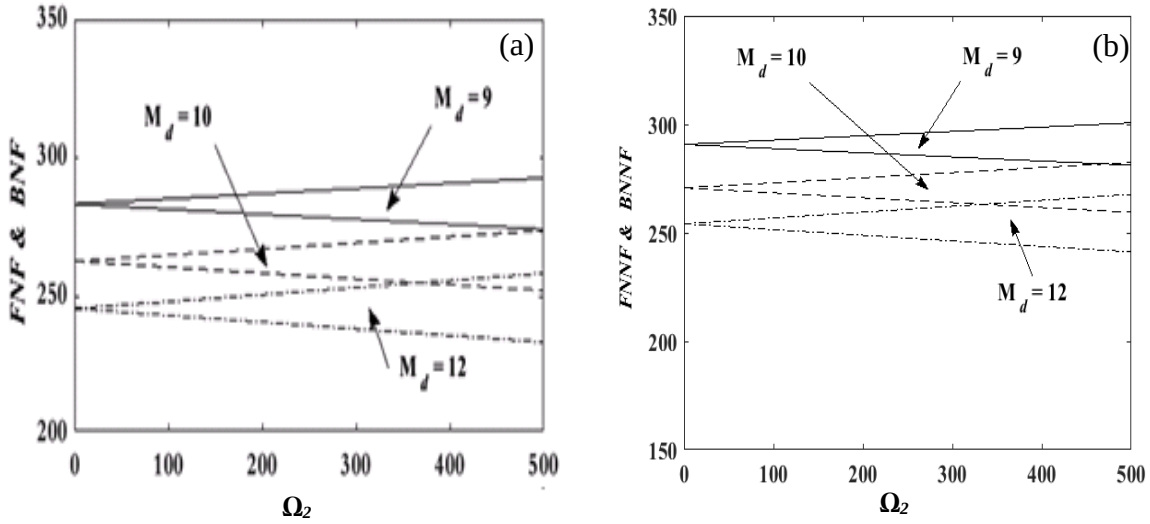

Fig. 3.8: Effect of a mass of the disk on the both linear and nonlinear forward and backward natural frequencies

Figure 3.8 shows that with the increase in the disk mass, the effective mass of the system increases, and as a result, the natural frequencies are observed to be decreased. Moreover, the slope, i.e., $\partial N / \partial \Omega_2$ remains same irrespective of the disk mass. A constant change in the amplitude has been noticed when the geometric nonlinearity has been introduced. However, the difference between the frequencies keeps constant with the change in the mass of the disk. Apart from this, the critical speed almost maintains at a constant value and it fluctuates between 250 to 300 *rad/s*. The effect of changing the shaft radius on the critical speeds is demonstrated in Fig.3.9. Here, one may notice that with an increase in the shaft radius, the whirling speed significantly increases while both the forward and backward natural frequencies coalesce almost to a single value for a higher shaft radius. When the external excitation corresponds with one of the critical speeds, the system undergoes a response with high amplitude in both the directions. Further, the nonlinear natural frequencies have greatly been influenced by the radius of the shaft and are observed to be higher slope, i.e., $\partial N / \partial \Omega_2$ for a moderately high value of the shaft radius. Therefore, the evaluation of a Campbell diagram exhibits the insight picture of the critical speed of the rotor-bearing system when the geometry of the rotor shaft is being varied. The geometric changes may cause a catastrophic failure if the system is operated at a frequency equal to that of one of the critical speeds for the same material property. Hence, the operator must ensure that the running speed must not meet one of the resultant critical speeds for every distinct configuration of the rotor geometry to avoid a sudden catastrophic failure.

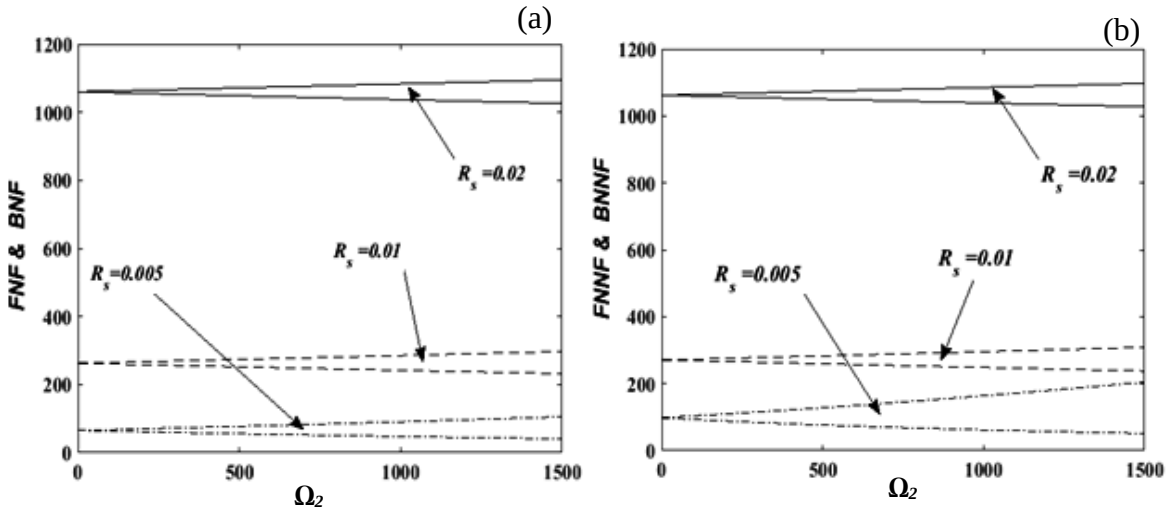

Fig.3.9: Effect of the shaft diameter on both linear and nonlinear forward and backward natural frequencies with the disk

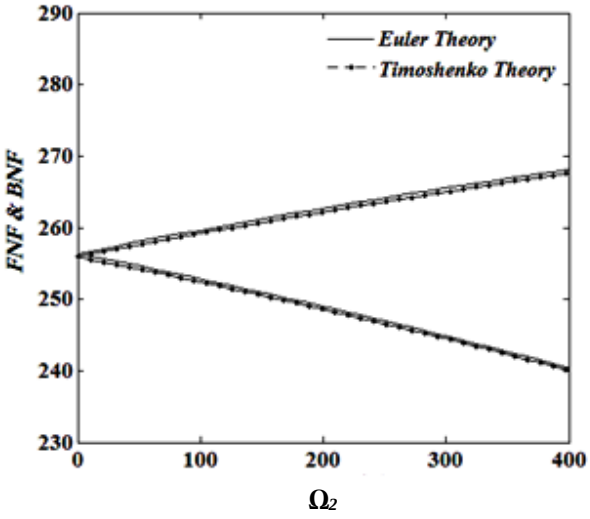

Fig.3.10 : Linear forward and backward natural frequencies using the Euler and Timoshenko theory; *L=0.5m*

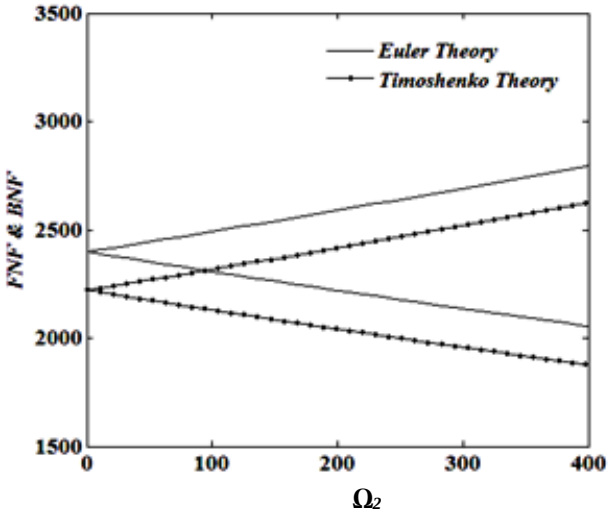

Fig.3.11: Linear forward and backward natural frequencies using the Euler and Timoshenko theory; *L=0.06m*

Figures 3.10-3.11 draw a comparison between the natural frequencies by taking both the Euler and Timoshenko beam models into account for the two shaft lengths equal to $0.5m$ and $0.15m$. It is observed that the differences of the whirling speeds between these two models are found to be negligible for the shaft length equal to $0.5m$. But, when a length of the shaft becomes less than $0.15m$, then difference of the results is noticeable. Therefore, the effect of shear deformation and rotary inertia is negligible for the shaft length $L \geq 0.15$ m. Hence, the present model derived based on the Euler theory is itself sufficient to predict a correct value of the critical speeds and the dynamic responses under various similar working conditions for the shaft length $L \geq 0.15$ m.

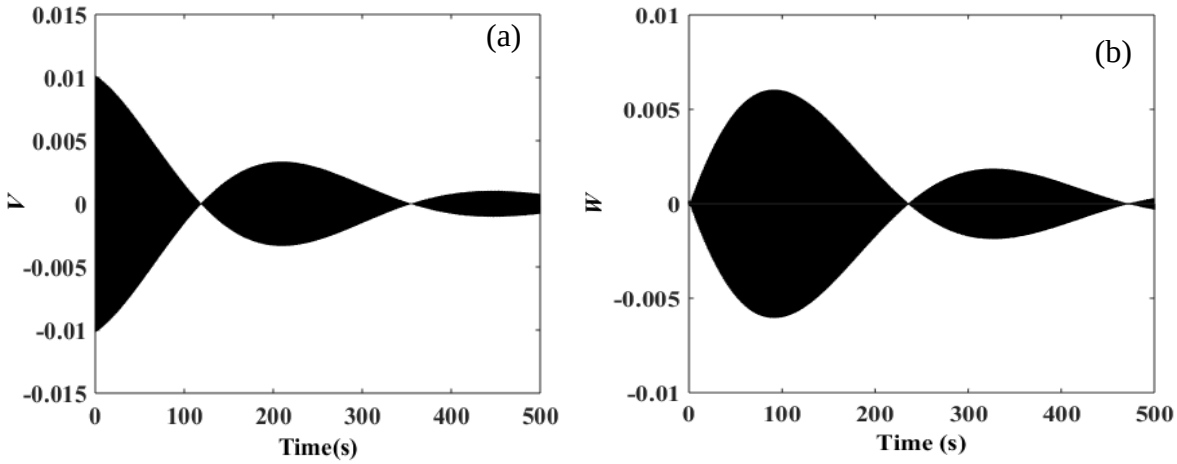

Fig. 3.12: Time history of the free vibration of *v* (→ *Y*) and *w* (→ *Z*) directions.

Figure 3.13 shows the time history for V and W under initial conditions $V = 0.01$, $\dot{V} = 0.0$, $W = 0.0$, and $\dot{W} = 0.0$. It is observed that even though the rotor-bearing system is being excited in the X – Y plane, the vibration, however, strongly exists in other directions also due to strongly nonlinear coupled terms, i.e., V^3+VW^2 and W^3+WV^2. Further, the amplitude of vibration stabilizes quickly in the orthogonal direction $(W \rightarrow Z)$ than the time taken in the excited direction $(V \rightarrow Y)$

b. ***Nonlinear Phenomenon: Chaotic Behavior***

Some critical observations to illuminate the presence of nonlinear phenomena accompanied with chaotic behavior or route to chaos have been studied upon gradually varying the design parameters.

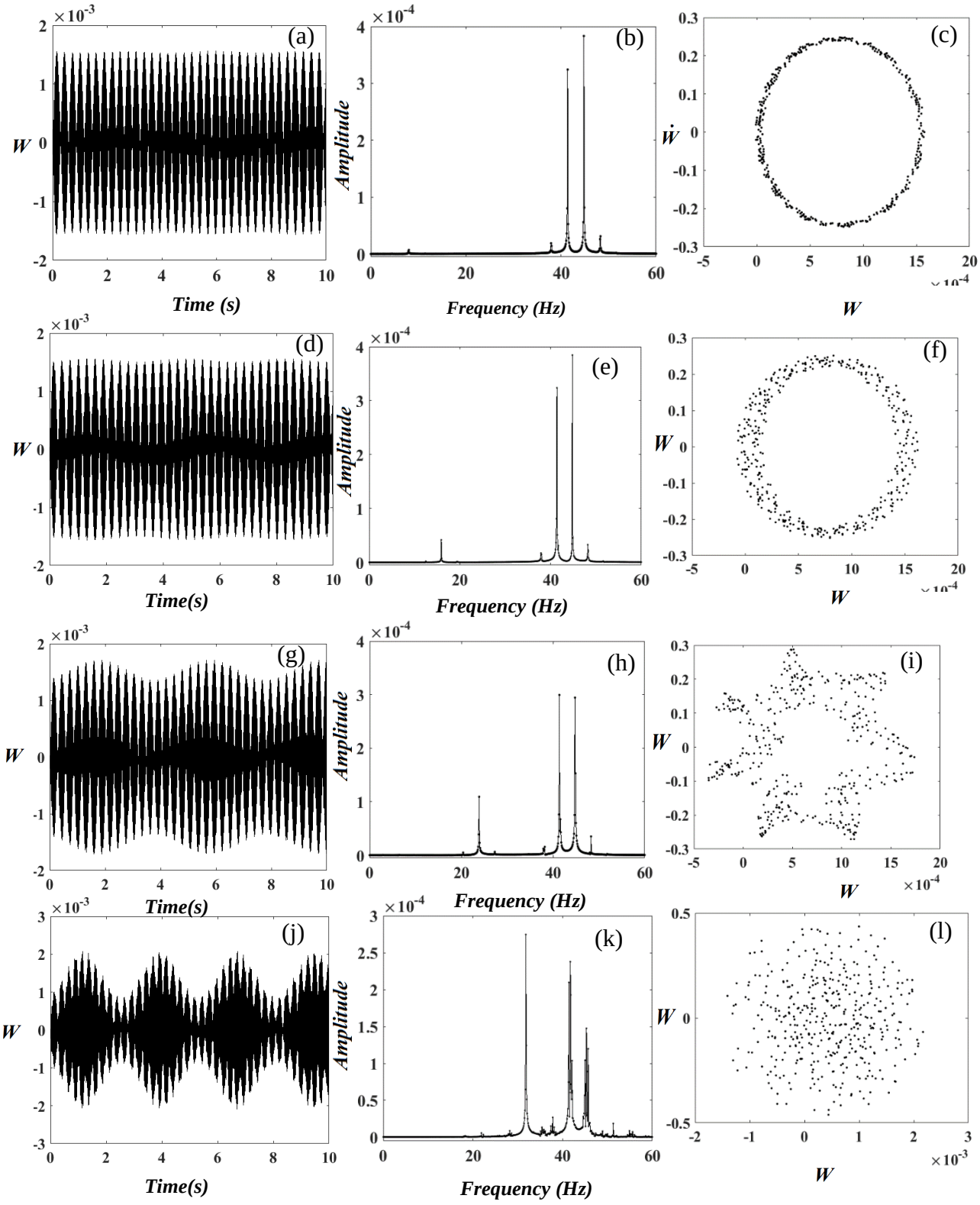

Fig.3.13: Effect of external frequency (Ω_2) on the dynamic performances of the rotor-bearing system; M_e=*0.12 kg*,

These graphical observations have been obtained by numerically integrating Eqs.(3.90)-(3.91) with the initial conditions $V(0)=0.01$, $\dot{V}(0)=0$, $W(0)=0$, and $\dot{W}(0)=0$, moreover these are portrayed in Fig.3.13 -3.15. An effect of the shaft spins speed (Ω_2) on the dynamic behavior is illustrated in Fig.3.13 through a time history, Fourier spectrum and Poincare's map. The time history has been transformed into the frequency domain, i.e., Fourier spectrum to closely observe the nature of responses which may enable to interpret the critical value of control parameters dealing with the chaotic behaviors, as shown in Fig.3.13(i). However, here, the route to chaos has clearly been visible and clearly depicted in the Poincare's map combined with the FFT for a wide range of the shaft spin speed. Incommensurate relation between the natural frequencies and the rotational speed has been found and leads a quasi-periodic motion clearly evident by a closed curve in the Poincare's map as shown in Fig.3.13(c) rather aperiodic motion when the spin speed is 50 rad/s. As the rotational speed increases from 50 to 250 rad/s, the closed curve in the Poincare's map that characterizes a quasi-periodic motion and period doubling as depicted in Fig.3.13(*f*) become distorted and finally breaks into torus doubling resulting in a chaos. When the spin speed becomes closer to either one of the natural frequencies, the points in the Poincare's map appear as a cloud unorganized points in the state space rather than a closed orbit which represents indeed a chaotic shown in Fig.3.13(*l*). Furthermore, a strong connection between the spin speed and the natural frequencies has been qualitatively observed, and as the control parameter increases, the torus shape becomes distorted and looks like a hexagonal in Fig.3.13(*i*). This change may be happened as the torus grows and gets closed to the six fixed points corresponding to a period-6 saddle orbit. Hence, the spin speed of the shaft strongly exhibits the chaotic nature of behaviors when its value reaches to one of the critical natural frequencies and externally induced frequency from the ground motion.

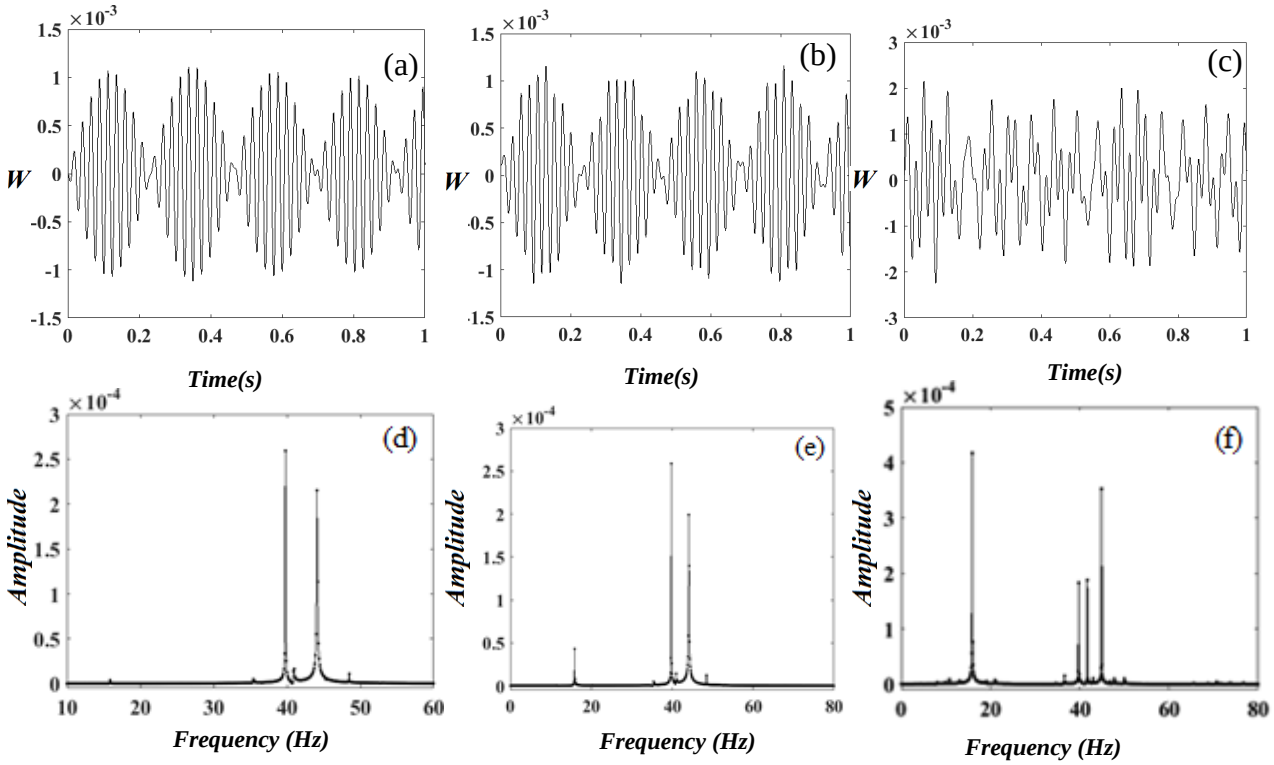

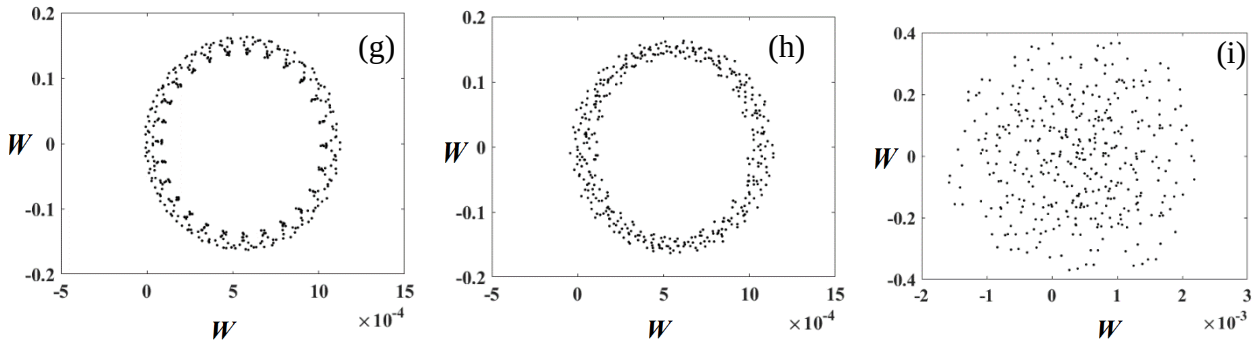

Fig.3.14: Effect of external amplitude (Z_a) on the dynamic performances of the rotor-bearing system.

Influences of external amplitude (Z_a) on nonlinear characteristics have been investigated by demonstrating time history, FFT and Poincare's map for Z_a equal to (0.001, 0.005, 0.01) *mm* in Fig.3.14. A quasi-periodic scenario followed by a chaotic behavior is strongly exhibited when the amplitude of excitation (Z_a) is being varied. For a low value, a quasi-periodicity occurs due to the presence of Hopf bifurcation supported by the presence of incommensurate frequencies which are clearly depicted in Fourier spectrum. As the Z_a increases, transition to chaos from the quasi-periodic motion through the distortion of torus shape has been observed. Hence, the external amplitude may play a decisive factor whether to make the system stable by controlling its magnitude (Fig.3.14).

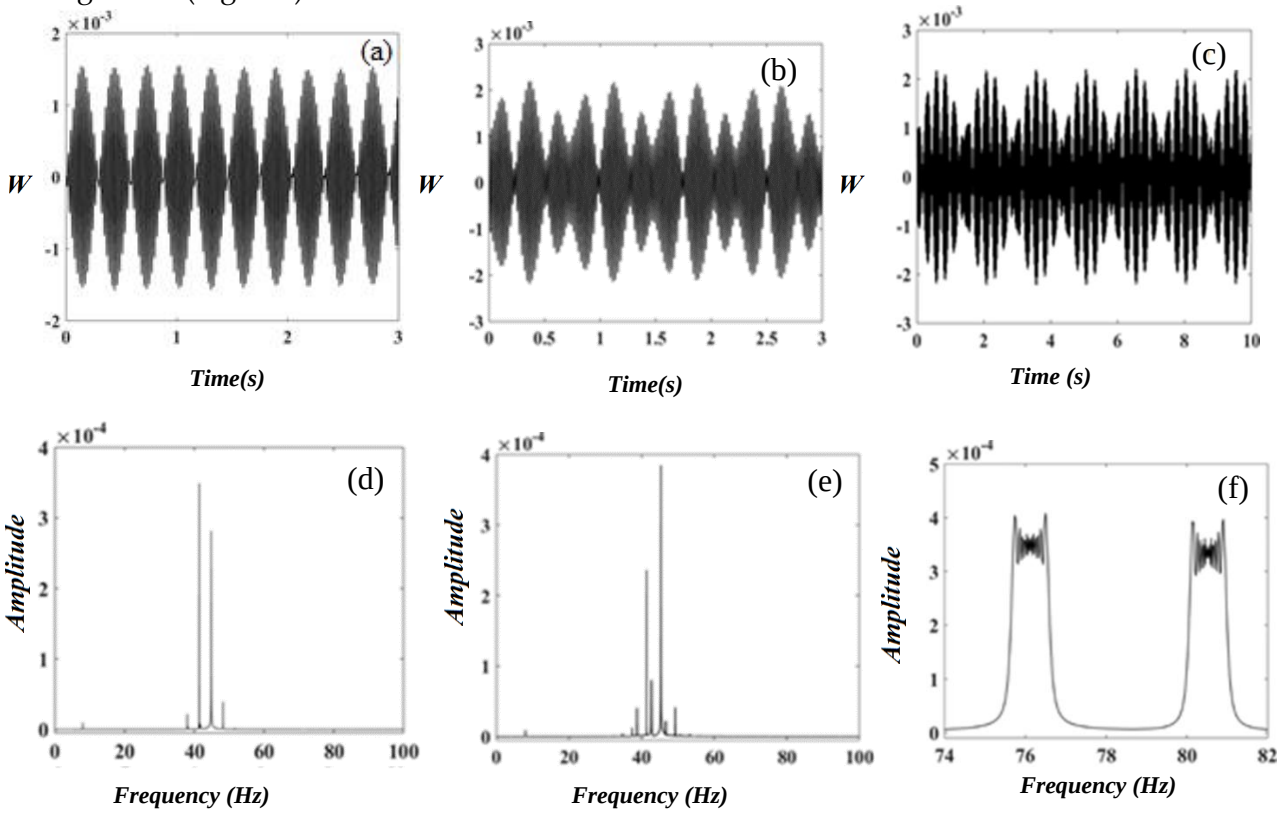

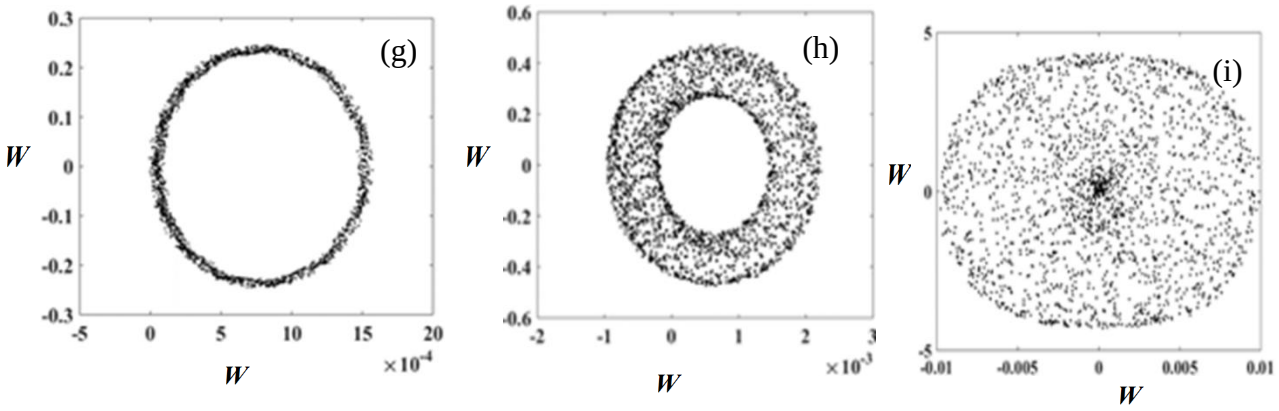

Fig. 3.15: Effect of initial conditions on the dynamic performances of the rotor-bearing system.

Thus, it has been observed that the chaotic behavior exists when the control parameter passes through its critical value. Therefore, small changes in the initial conditions may result widely diverging outcome, and hence, sensitivity of choosing the initial conditions may play a crucial role to investigate the diverging behavior of highly coupled a nonlinear rotor-bearing system. Thus, here the effect of initial conditions on the dynamic behaviors has been demonstrated through a time history, FFT and Poincare's map as shown in Fig. 3.15 It has been noticed that while one set of the initial condition provides a deterministic behavior with no random components involved, the same configuration may results the futuristic behavior as deterministic chaos under other initial condition.

c. *Frequency Responses: Steady State Solutions*

For ensuring a safe, smooth and effectual operation, it is considerably important to have a very good understanding of the steady-state solutions and auxiliary bifurcations of the system embraced with essential features. Here, a relation between vibration amplitude and external frequency of the steady-state rotor-bearing system has been obtained to render some interesting design guidelines and suggestions about the operational flexibilities. The steady-state behavior has been explored over a wide range of the parametric configurations for three distinct resonant conditions. The effect of various control parameters on the vibration amplitude has been discussed when the external excitation is matching with one of the system natural frequencies. While solid lines in the frequency response curves represent stable/bounded solutions, dotted lines represent the unstable/unbounded solutions. It can be observed that the effect of nonlinearity causes the frequency curves to bend rightwards from the position of the linear response. This phenomenon is generally known as hardening spring behavior as the response curve becomes asymmetric and inclined towards higher frequencies. In order to empathize the control behaviors as a result of varying of design parameters, two resonance conditions, i.e., $\omega_e \approx \omega_1$, *and* $\omega_e \approx \omega_2$, have been considered, while resonance condition $\omega_e \approx \omega_1$ has been selected to comprehend the behavioral effect of mass imbalance.

I. Effect of amplitude of ground disturbance

Figure 3.16 illustrates the effect of amplitude of ground motion Z_0 equal to 0.01 m, 0.001 m and 0.0001m on the frequency response curves when the external frequency is nearly equal to the forward whirl speed $\{\omega_e \approx \omega_1\}$ and the backward whirl speed $\{\omega_e \approx \omega_2\}$. It is noted that the saddle–node bifurcation gets shifted towards a right to cover a greater range of the external frequency (σ) when amplitude of the external excitation increases. Amplitude of the vibration gets higher with an increase in the magnitude of the external excitation. With an increase in the magnitude of the ground excitation, S–N bifurcation which is accountable for jump-up phenomena starts at a higher frequency while the jump length, i.e., a length indicating the jump of amplitude, gets

escalated. With increase in the magnitude of the excitation, the S–N bifurcation is gradually disappeared from the frequency response curves, and the system becomes SISO, i.e., single input–single output, while for a low value of the amplitude, the system can be, however, brought down to the equivalent linear system

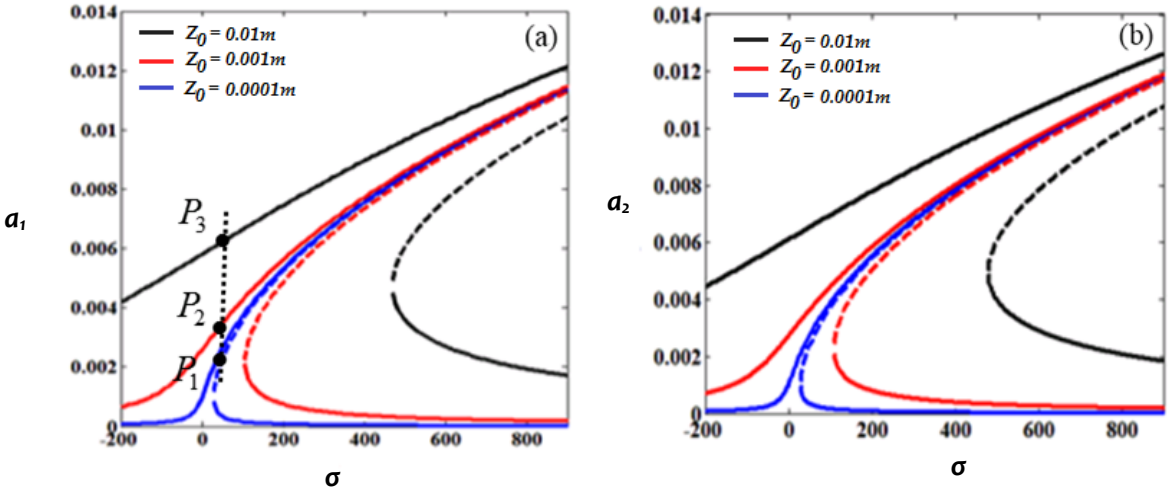

Fig. 3.16: Influence of external amplitude on the frequency response curves.

II. Effect of disk location

Figure 3.17 shows an effect of the disk position L_d equal to 0.2 m, 0.166 m and 0.1 m from the one of the bearing ends on the frequency response characteristic. The resonant curves show more strongly bending towards the right when the disk moves away from the mid-position of the shaft. The vibration amplitude gets its maximum when the disk is at a mid-point. It is noteworthy to observe that while maximum amplitude remains nearly the same for $\omega_e \approx \omega_1$, the amplitude of vibration gets decreased for $\omega_e \approx \omega_2$ with the variation of disk location considering the same system configuration. While the bifurcation point remains unaltered, the jump length reduces as the disk moves away from the mid-position. Hence, the chances of catastrophic failure due to a sudden jump can be attenuated by repositioning of the disk.

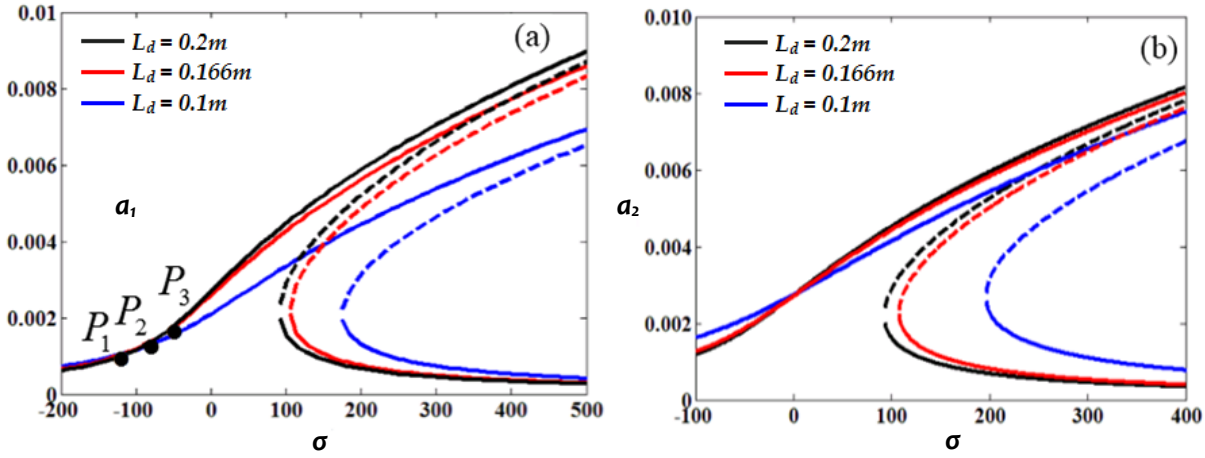

Fig.3.17: Variation of a location of the disk on the frequency response curves.

III. Effect of mass of the disk

Figure 3.18 demonstrate es an effect of the disk mass M_d equal to (9, 10.5, 12) kg to interpret the advance indication of instability due to bifurcation. A similar nature of the resonant curves has been, however, observed and bends more strongly towards the right as the mass of the disk increases. With an increase in the disk masses, the response amplitude gets increased while a minimal impact on jump length as it remains constant for nearly all values of the disk mass. It

has also been observed that the jump phenomena start at the frequencies within a narrow range $105 \leq \sigma \leq 125$.

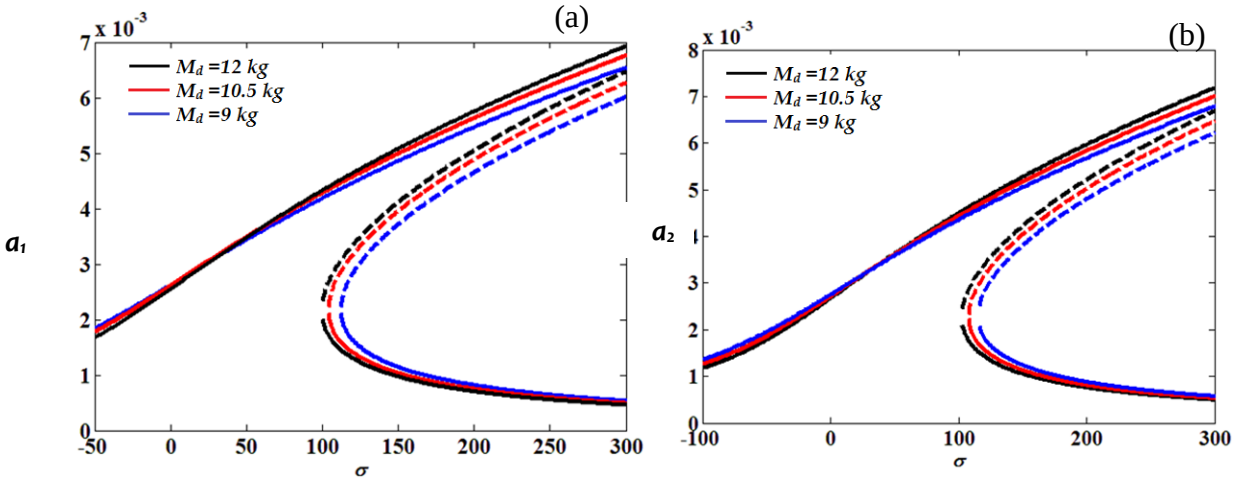

Fig.3.18: Variation of a mass of the disk on the frequency response curves.

.

IV. Effect of shaft radius

The effect of shaft radius to investigate the steady state behavior for the shaft radius equal to (0.02, 0.01, and 0.005) m has been illustrated in Fig.3.19. It is observed that the resonant curves are flexed towards the higher frequency when the shaft radius is altered. As the shaft radius increases, the amplitude of responses gets increased. Further, the jump-up phenomena is almost disappeared for a narrow shaft. As a result, the flexible rotor-bearing system can be simplified with a linear model comprising discrete spring-mass-damper elements when the shaft radius becomes small. In addition, it is noteworthy that since the bifurcation starts at higher external frequency, the system can safely operate under frequency range $\sigma \leq 250$, and hence, chances of catastrophic failure due to the S–N bifurcation may reduce with increase in a radius of the shaft

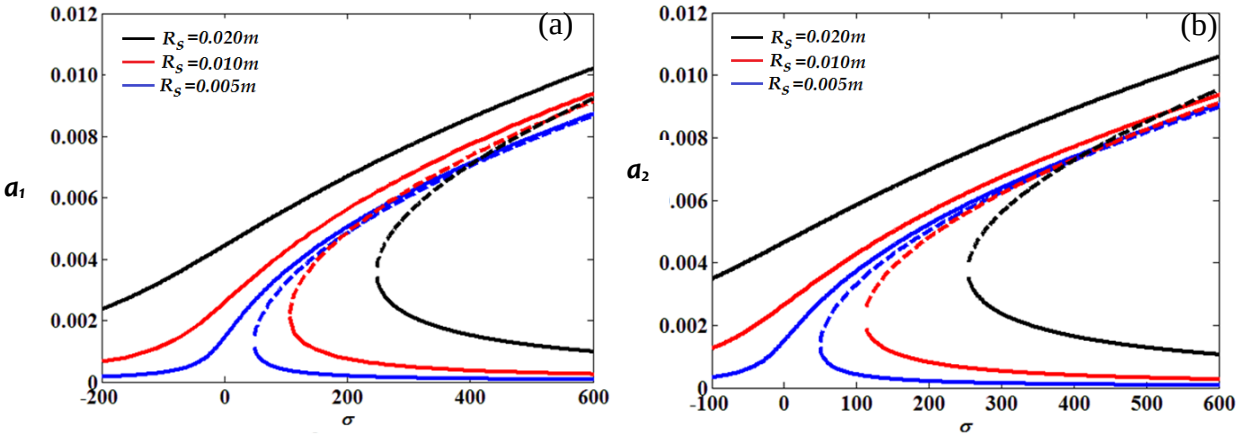

Fig.3.19: Variation of radius of the shaft on the frequency response curves.

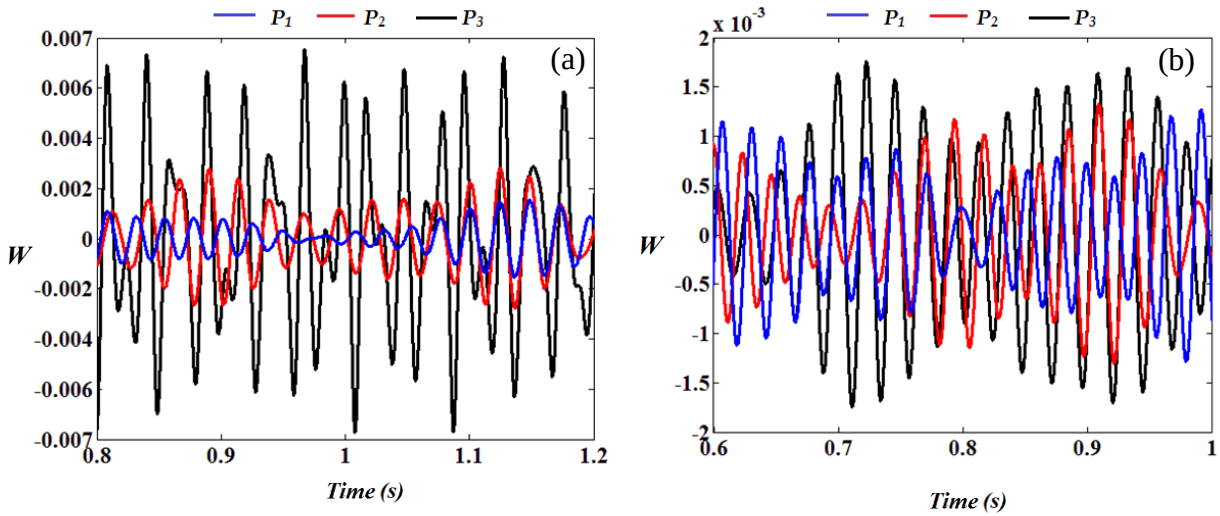

Fig.3.20: (a) Time history and phase portrait at the pointsP_1, P_2, P_3 (Fig. **3.16**) (b) Time history (3.17)

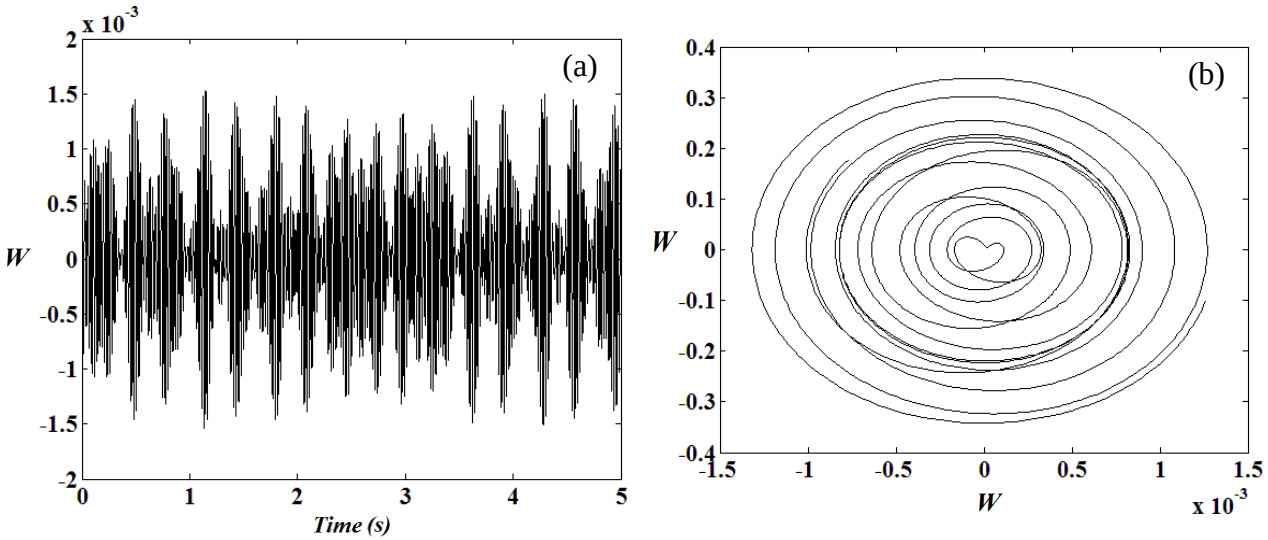

Fig.3.21: Time history and phase portrait at the point (Fig. 3.16) with initial point 0.001, 0.001.

However, the results obtained using first-order MMS are validated with the results obtained by numerically solving the temporal equations of motion at the various points indicated in Fig. 3.16. Time responses are illustrated in Fig.3.20 and Fig.3.21 at points (P_1, P_2, P_3) considering same parameters' values as that of chosen while obtaining Fig. 3.16. An error within the range of 5–9% has been found while determining the steady-state response from the equation of motion numerically as compared to the amplitude of vibration depicted in Fig. 3.16 and Fig. 3.17. It may thus clearly be observed that the amplitude of the steady-state time responses obtained by numerically solving the temporal equation of motion is found to be in the same range with that obtained by using the perturbation method (Fig. 3.16 and Fig. 3.17).

V. Effect of mass imbalance

As a result of varying the mass of imbalance (m_u), the steady-state responses have been studied for the mass imbalance equal to (0.001, 0.01, 0.1) kg, while other parameters such as Z_d= 0.001, L_d= L/3 and M_d=10.5 kg keep constant. With increase in m_u, an amplitude of the vibration increases since the forcing amplitude ($m_u\Omega_2^2\mu_1\varphi\{L_d\}$) gets increased with increase in the mass imbalance, and the system becomes considerably high forced induced vibration. As a result, the jump phenomena are found to be invisible for a wide range of frequency. One can undermine the effect

(a) (b)

of nonlinearity and bring down the system with stable nontrivial response where the amplitude linearly varies with an increase in the frequency of the ground motion. However, there is no significant change in the jump length, so that the catastrophic failure due to a sudden jump can be ignored as indicated in Fig.3.22

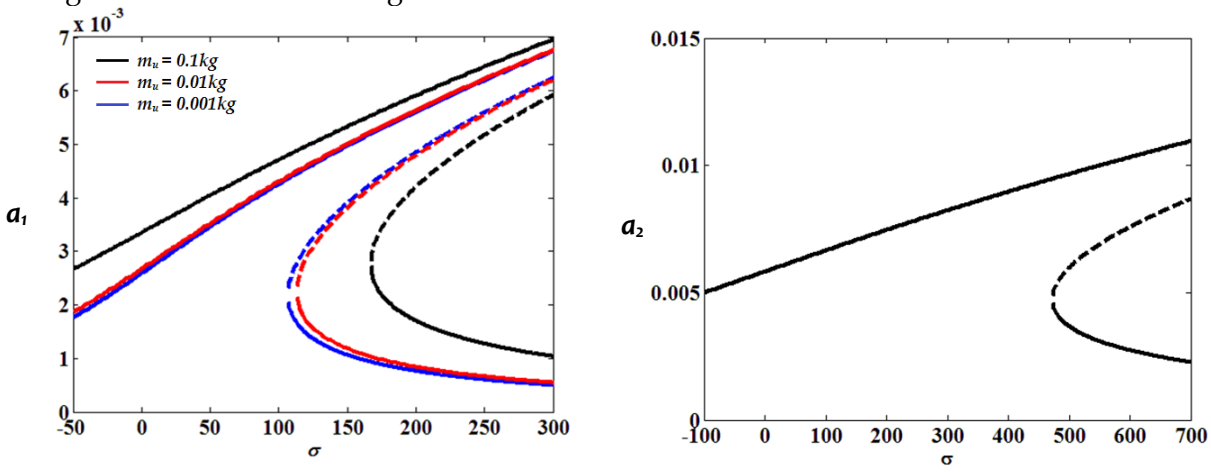

Fig.3.22: Effect of Mass unbalance (m_u) on the frequency response curves.

3.4 Excitation of an axial loading and an unbalance mass

Unavoidable axial loading on a rotating system also appears in many rotating machines. The axial loading in the rotating machines are due to many reasons such as the use of helical gear train in the gearbox, a load from the blower fan/compressor fan, hydraulic axial load in turbines, loading in drilling, milling, and boring operations, thrust force in jet engines and many special purpose industrial applications. The axial loading causes the parametric excitation of the system. It shows different resonance conditions than that of the conventional resonance such that the system vibrates at a half of the excitation frequency.

In this section, an investigation of the stability and bifurcation of a nonlinear rotor-disk system supported by flexible bearings under combined effect of a mass unbalance and a pulsating axial force is performed. One of the shaft ends is roller supported so, there is no effect of axial stretching. Thus, the nonlinearity due to the large deformation only is considered here.

3.4.1 Analysis

A schematic diagram of a rotating system for this study is represented in Fig.3.23 with a hinge-roller support. The rotor is modeled as a uniform flexible shaft with length (l) and radius (R_s), a rigid disk with thickness (h) and radius (R_d), which is located at a distance (l_d) along the shaft span from one of the ends. The rotor is supported at the ends by the flexible bearings. A pulsating compressive force i.e., $P_0+P_1cos\ (\Omega_1 t)$ is applied axially at the rear end of the shaft.

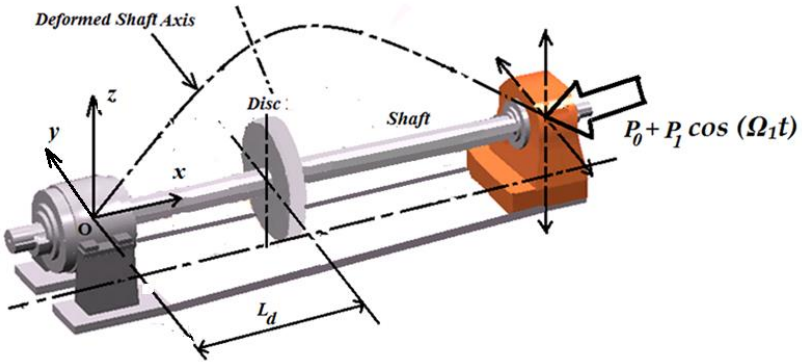

a)

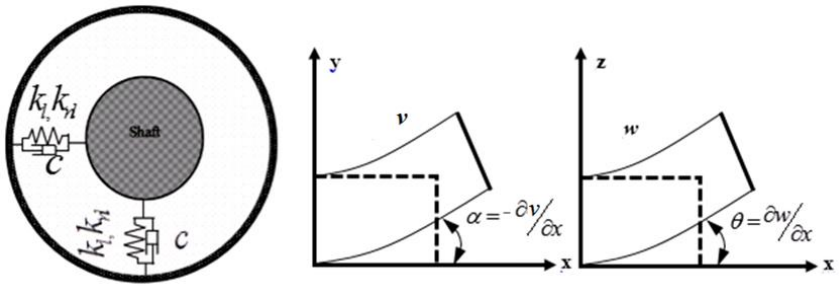

b)

Fig.3.23: a) A shaft disk system subjected to axial load **b)** Equivalent linear and nonlinear spring-damper system; State of elastic deformation in transverse direction (y, z)

The total potential energy of the rotor system can now be expressed as

$$U=\int_0^l\left(\frac{EI}{2}\right)\left\{\left(\frac{\partial}{\partial x}\left(\frac{\partial v}{\partial x}\right)\right)^2+\left(\frac{\partial}{\partial x}\left(\frac{\partial w}{\partial x}\right)\right)^2\right\}dx+\int_0^l\left(\frac{EA}{8}\right)\left\{\left(\frac{\partial v}{\partial x}\right)^4+\left(\frac{\partial w}{\partial x}\right)^4+2\left(\frac{\partial v}{\partial x}\right)^2\left(\frac{\partial w}{\partial x}\right)^2\right\}dx \qquad (3.97)$$

Work done due to non-conservative forces respectively can be written as

$$W_p=\frac{1}{2}\int_0^l\left(P_0+P_1\cos(\Omega_1 t)\right)\left(v'^2+w'^2\right)dx. \qquad (3.98)$$

Here Ω_1 is frequency of the dynamic pulsating axial force P_1 while a direction and position of the axial force as shown in Fig.3.23. Work done due to the non-conservative forces respectively can be written as

$$W_p=F_5\left(P_0+P_1\cos(\Omega_1 t)\right)\left(V^2+W^2\right).$$
$$\text{Where,}\qquad F_5=\frac{1}{2}\int_0^l\varphi'^2\,dx. \qquad (3.99)$$

Thus, the Eqs. (3.55) and (3.56) can be further written as,

$$\ddot{V}-\Omega_2\vartheta_1\dot{W}+\vartheta_2 V+\vartheta_3\left(P_0+P_1\cos\Omega_1 t\right)V+\left\{\left(\vartheta_4+\frac{\mu_1}{2}\right)V^3+\frac{\mu_1}{2}VW^2\right\}+c\dot{V}$$
$$=m_u\Omega_2^2 r\varphi\left(l_d\right)\cos\Omega_2 t, \qquad (3.100)$$

$$\ddot{W}+\Omega_2\vartheta_1\dot{V}+\vartheta_2 W+\vartheta_3\left(P_0+P_1\cos\Omega_1 t\right)W+\left\{\left(\vartheta_4+\frac{\mu_1}{2}\right)W^3+\frac{\mu_1}{2}WV^2\right\}+c\dot{W}$$
$$=m_u\Omega_2^2 r\varphi\left(l_d\right)\sin\Omega_2 t. \qquad (3.101)$$

Here $\vartheta_3=F_5/a_1$, it has been observed that the equations of motion consist the parametrical excitation term (i.e P_0+P_1 $cos(\Omega_1 t)$) due to the axial loading and forcing terms (i.e., $m_u\Omega_2^2 r\varphi(l_d)$) due to the mass unbalance. Since the governing equations of motion consist the nonlinear terms, the exact solutions are somehow difficult to determine. Therefore, an approximate solution for the system of equation can be determined by using the perturbation approach. Similar treatment of the method of multiple scales as described in the previous section is adopted for Eqs.(3.100)-(3.101). Then, it results into following equations for order 1 of ε.

$$\frac{\partial^2 V_1}{\partial T_0^2}+(\vartheta_2+\vartheta_3 P_0)V_1-\Omega_2\vartheta_1\frac{\partial W_1}{\partial T_0}=$$
$$\left[iD_1\Omega_2\vartheta_1 A_1-2i\omega_1 D_1 A_1-i\omega_1 cA_1-(2\mu_1+4\vartheta_4)A_1{}^2\bar{A}_1-4\mu_1 A_1 A_2\bar{A}_2\right]\exp(i\omega_1 T_0)-$$
$$\left[-iD_1\Omega_2\vartheta_1 A_2-2i\omega_2 D_1 A_2-i\omega_2 cA-4\mu_1 A_1 A_2\bar{A}_1-(2\mu_1+4\vartheta_4)A_2{}^2\bar{A}_2\right]\exp(i\omega_2 T_0)$$
$$-\frac{1}{2}\vartheta_3 A_1 P_1\left\{\exp(i\Omega_1 T_0)+\exp(-i\Omega_1 T_0)\right\}\exp(i\omega_1 T_0)$$
$$-\frac{1}{2}\vartheta_3 A_2 P_1\left\{\exp(i\Omega_1 T_0)+\exp(-i\Omega_1 T_0)\right\}\exp(i\omega_2 T_0)$$
$$+\frac{1}{2}\Lambda\left(\exp(i\Omega_2 T_0)+\exp(-i\Omega_2 T_0)\right)+[cc]. \tag{3.102}$$

$$\frac{\partial^2 W_1}{\partial T_0^2}+(\vartheta_2+\vartheta_3 P_0)W_1+\Omega\vartheta_1\frac{\partial V_1}{\partial T_0}=$$
$$\left[2\omega_1 D_1 A_1+\omega_1 cA_1-\Omega_2\vartheta_1 D_1 A_1-(2\mu_1+4\vartheta_4)iA_1{}^2\bar{A}_1-4i\mu_1 A_1 A_2 A_2\right]\exp(i\omega_1 T_0)+$$
$$\left[-2\omega_2 D_1 A_2-\omega_2 cA_2-\Omega_2\vartheta_1 D_1 A_2+4i\mu_1 A_1 A_2\bar{A}_1+(2\mu_1+4\vartheta_4)iA_2{}^2\bar{A}_2\right]\exp(i\omega_2 T_0)$$
$$-\frac{1}{2}i\vartheta_3 A_1 P_1\left\{\exp(i\Omega_1 T_0)+\exp(-i\Omega_1 T_0)\right\}\exp(i\omega_1 T_0)$$
$$-\frac{1}{2}i\vartheta_3 A_2 P_1\left\{\exp(i\Omega_1 T_0)+\exp(-i\Omega_1 T_0)\right\}\exp(i\omega_2 T_0)$$
$$+\frac{1}{2}i\Lambda\left(\exp(-i\Omega_2 T_0)-\exp(i\Omega_2 T_0)\right)+[cc]. \tag{3.103}$$

It may be noted from Eqs.(3.102) - (3.103) that it may contain the secular or small divisor terms when the system is subjected to resonance conditions: (*i*) $\Omega_1 = 2\omega_1$, (ii) $\Omega_1 = 2\omega_2$, (iii)$\Omega_2 = \omega_1$and $\Omega_1 = 2\omega_1$, and (iv) $\Omega_2 = \omega_2$and $\Omega_1 = 2\omega_2$. The system shows almost similar behavior for the resonance conditions corresponding to ω_1 and ω_2. Thus, the resonance conditions are explored only corresponding to ω_1 and discussed in the following subsection.

Resonance condition $\Omega_1 \approx 2\omega_1$:

The procedures explained in the previous section and substituting the expression $\Omega_1 = 2\omega_1 + \sigma_1\varepsilon$, where σ_1 is a small detuning parameter and $A_n = (1/2)a_n\, exp(i\varphi_n)$, n = 1, 2 in the resulting equations and separating the real and imaginary part, one may obtain an autonomous system of four first order partial differential equations, which have been expressed as

$$(4a_1\phi_1')\left(\Omega_2^2\omega_1\vartheta_1{}^2-\Omega_2 P_0\vartheta_1\vartheta_3-\Omega_2\omega_1{}^2\vartheta_1-\Omega_2\vartheta_1\vartheta_2+2P_0\omega_1\vartheta_3-2\omega_1{}^3+2\omega_1\vartheta_2\right)+$$
$$2a_1 a_2{}^2\left(\omega_1\Omega_2\vartheta_1-P_0\vartheta_3+\omega_1{}^2-\vartheta_2\right)(2\mu_1+3\vartheta_4)+a_1{}^3\left(\omega_1\Omega_2\vartheta_1-P_0\vartheta_3+\omega_1{}^2-\vartheta_2\right)$$
$$(2\mu_1+3\vartheta_4)=2a_1 P_1\cos(\alpha)\left(\vartheta_3\omega_1{}^2-\vartheta_3{}^2P_0-\vartheta_3\vartheta_2-\omega_1\Omega_2\vartheta_1\vartheta_3\right). \tag{3.104}$$

$$(a_1')\left(\Omega_2^2\omega_1\vartheta_1{}^2-\Omega_2 P_0\vartheta_1\vartheta_3-\Omega_2\omega_1{}^2\vartheta_1-\Omega_2\vartheta_1\vartheta_2+2P_0\omega_1\vartheta_3-2\omega_1{}^3+2\omega_1\vartheta_2\right)+$$
$$ca_1\left(-\Omega_2\omega_1{}^2\vartheta_1+P_0\omega_1\vartheta_3-\omega_1{}^3+\omega_1\vartheta_2\right)=a_1 P_1\sin(\alpha)\left(\vartheta_3{}^2P_0-\vartheta_3\omega_1{}^2+\vartheta_3\vartheta_2+\omega_1\Omega_2\vartheta_1\vartheta_3\right). \tag{3.105}$$

$$(4a_2\phi_2')\left(-\Omega_2^2\omega_2\vartheta_1{}^2-\Omega_2 P_0\vartheta_1\vartheta_3-\Omega_2\omega_2{}^2\vartheta_1-\Omega_2\vartheta_1\vartheta_2-2P_0\omega_2\vartheta_3+2\omega_2{}^3-2\omega_2\vartheta_2\right)+$$
$$\left(\omega_2\Omega_2\vartheta_1+P_0\vartheta_3-\omega_2{}^2+\vartheta_2\right)(2\mu_1+3\vartheta_4)\left\{2a_1{}^2a_2+a_2{}^3\right\}=0. \tag{3.106}$$

$$a_2'\left(-\Omega_2^2\omega_2\vartheta_1{}^2-\Omega_2 P_0\vartheta_1\vartheta_3-\Omega_2\omega_2{}^2\vartheta_1-\Omega_2\vartheta_1\vartheta_2-2P_0\omega_2\vartheta_3+2\omega_2{}^3-2\omega_2\vartheta_2\right)$$
$$+ca_2\left(-\Omega_2\omega_2{}^2\vartheta_1-P_0\omega_2\vartheta_3+\omega_2{}^3-\omega_2\vartheta_2\right)=0. \tag{3.107}$$

Here, $\alpha_1 = -2\phi_1 + \sigma_1 T_1$.One may set up $a_1' = 0$, and $\alpha' = 0$ to obtain the steady state response. Both trivial ($a=0$) and nontrivial ($a\neq 0$) solutions are then used to study the stability of the steady state responses by replacing a_1, and α_1 with $a_{10} + a_1'$and $\alpha_{10} + \alpha_1'$, respectively into Eqs. (3.104)-

(3.107) and then investigating the eigenvalues of the resulting Jacobian matrix (*J*) for further stability analysis.

Resonance condition $\Omega_1 \approx 2\omega_1$ and $\Omega_2 \approx \omega_1$:

Considering this resonance condition, the autonomous system of four first order partial differential equations can be expressed as following using the similar procedure as explained earlier.

$$\begin{aligned}&\left(4a_1\phi'\right)\left(\omega_1^{\,3}\vartheta_1^{\,2}-P_0\omega_1\vartheta_1\vartheta_3-\omega_1^{\,3}\vartheta_1+2P_0\omega_1\vartheta_3-2\omega_1^{\,3}-\omega_1\vartheta_1\vartheta_2+2\omega_1\vartheta_2\right)+\\&\left(\omega_1^{\,2}\vartheta_1-P_0\vartheta_3+\omega_1^{\,2}-\vartheta_2\right)(2\mu_1+3\vartheta_4)\left\{2a_1a_2^{\,2}+a_1^{\,3}\right\}=\\&\left(\omega_1^{\,2}-\vartheta_3P_0-\vartheta_2-\omega_1^{\,2}\vartheta_1\right)\left\{2a_1\cos(\alpha_1)\vartheta_3P_1+\sin(\alpha_2)4m_1\omega_1^{\,2}r_1\varphi(l_d)\right\}.\end{aligned} \tag{3.108}$$

$$\begin{aligned}&2a_1'\left(\omega_1^{\,3}\vartheta_1^{\,2}-P_0\omega_1\vartheta_1\vartheta_3-\omega_1^{\,3}\vartheta_1+2P_0\omega_1\vartheta_3-2\omega_1^{\,3}-\omega_1\vartheta_1\vartheta_2+2\omega_1\vartheta_2\right)+\\&2ca_1\left(-\omega_1^{\,3}\vartheta_1+P_0\omega_1\vartheta_3-\omega_1^{\,3}+\omega_1\vartheta_2\right)=\\&\left(-\omega_1^{\,2}+\vartheta_3P_0+\vartheta_2+\omega_1^{\,2}\vartheta_1\right)\left\{a_1\sin(\alpha_1)\vartheta_3P_1-\cos(\alpha_2)2m_1r_1^{\,2}u_1\varphi(l_d)\right\}\end{aligned} \tag{3.109}$$

$$\begin{aligned}&\left(2a_2\phi'\right)\left(-\omega_1^{\,2}\omega_2\vartheta_1^{\,2}-P_0\omega_1\vartheta_1\vartheta_3-\omega_1\omega_2^{\,2}\vartheta_1-2P_0\omega_2\vartheta_3-\omega_1\vartheta_1\vartheta_2+2\omega_2^{\,3}-2\omega_2\vartheta_2\right)+\\&\left(\omega_2\omega_1\vartheta_1+P_0\vartheta_3-\omega_2^{\,2}+\vartheta_2\right)(2\mu_1+3\vartheta_4)\left\{2a_1^{\,2}a_2+a_2^{\,3}\right\}=0,\end{aligned} \tag{3.110}$$

$$\begin{aligned}&a_2'\left(2\omega_2^{\,3}-\omega_1^{\,2}\omega_2\vartheta_1^{\,2}-P_0\omega_1\vartheta_1\vartheta_3-\omega_1\omega_2^{\,2}\vartheta_1-2P_0\omega_2\vartheta_3-\omega_1\vartheta_1\vartheta_2-2\omega_2\vartheta_2\right)+\\&2ca_2\left(-\omega_1\omega_2^{\,2}\vartheta_1-P_0\omega_2\vartheta_3+\omega_2^{\,3}-\omega_2\vartheta_2\right)=0.\end{aligned} \tag{3.111}$$

Here,$\alpha_1 = -2\phi_1 + \sigma_1 T_1$ and $\alpha_2 = -\phi_1 + \sigma_2 T_1$. For sake of simplicity, the detuning parameters are assumed as $\sigma = \sigma_1 \approx \sigma_2$. A steady state solution has been obtained by setting up $a_2^{/} = 0$,. and $\alpha^{/} = 0$. Only non-trivial solutions are found to be exist and stability of these responses have been obtained by perturbing with $a_1 = a_{10} + a_1^{/}$, $\alpha_2 = \alpha_{20} + \alpha_2^{/}$and $\alpha_1 = \alpha_{10} + \alpha_1^{/}$. Investigating the eigenvalues from the resultant Jacobian matrix (*J*) renders the stability information while real part of eigenvalues of the *J* decides the destiny whether the system is under control with this working condition. Simultaneously, negative real part of all eigenvalues denotes asymptotically stable system while the presence of positive real part of an eigenvalue denotes unstable corresponding solution.

3.4.2 Result and Discussion

In the numerical simulations, we consider the rotor-disk-bearing system made up of steel material with the following material and geometric properties.

Parameters	**Value**	**Parameters**	**Value**
Shaft length	0.8 *m*	Modulus of elasticity	200 *GPa*
Shaft radius	0.01 *m*	Viscous damping	15 *Ns/m*
Disk radius	0.06 *m*	Linear bearing stiffness	2×10^5 *N/m*
Disk thickness	0.003 *m*	Nonlinear bearing stiffness	1×10^9 *N/m*^{3}
Unbalance mass	0.012 *kg*	Mass density	7800 *kg/m*^{3}
Eccentricity of the unbalance mass	0.06 *m*		

Table 3.1 : Parameters of a rotating model

We depicted the nature of deflection incurred generally under any dynamic loading condition or when the system is subjected to any resonance condition called as mode-shapes/Eigen spectrums. This mode shape has further used to demonstrate the overall dynamic performance and predict the accurate bifurcation in the frequency response curves that renders the critical operating condition. The predicted shapes of the deflected structure under free vibration or deflection pattern of the vibrating body subjected to the non-periodic excitations for the first and 2nd mode of vibration with and without the flexible bearings have been demonstrated in Fig.3.24. It compares the structural modes with the rigid and flexible supports. With the rigid bearings, it is often noticed that the deflection is found to be zero magnitude at the bearing end as compared with the flexible bearing where the flexible bearing is pertaining non-zero magnitude of the deflection at the bearing end. Thus, here, the deflection can be observed at the different points i.e., non-zero magnitude other than the ends point of the shaft. We consider similar mode shapes to evaluate the steady-state responses and further verified between approximate and numerical solutions. A clear non-trivial but steady vibration amplitude is observed at the flexible bearing ends when the combined system vibrates at its second resonance condition.

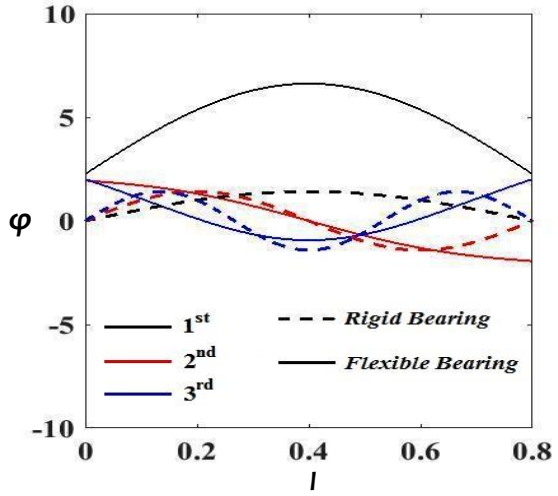

Fig.3.24: Mode shapes: a) Flexible bearing: λ1 = 3.45, λ2 = 5.34, λ3 = 7.14 b) Rigid bearing

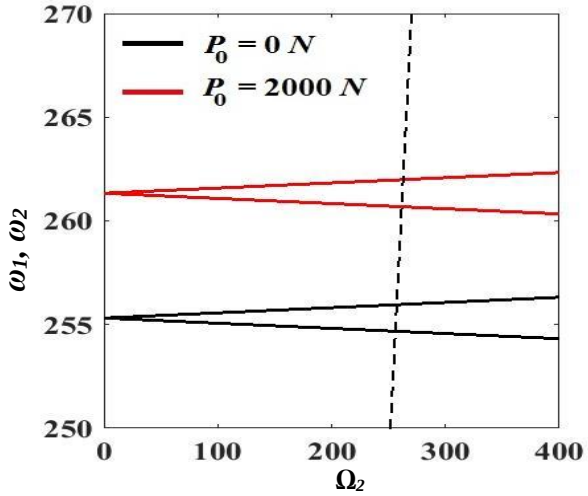

Fig.3.25: Campbell diagram : $l_d = l/4$, R_d= 0.08 m

Figure 3.25 portrays the characteristic behavior (i.e. the natural frequency) of the system against the change in the spin speed with an influence of the static axial force P_0. It has been observed that the P_0 directly contributes to a stiffness term of the equation of motion. The overall stiffness increases with an increase in the axial forces, and as a result the natural frequency is found to be increased. Hence, it has been observed that the axially compressive loaded shaft is found to be more stiffened and as a result, both the forward and backward critical frequencies have been moved to a higher value and as a result, increasing the axial loads ensure the stability of the system.

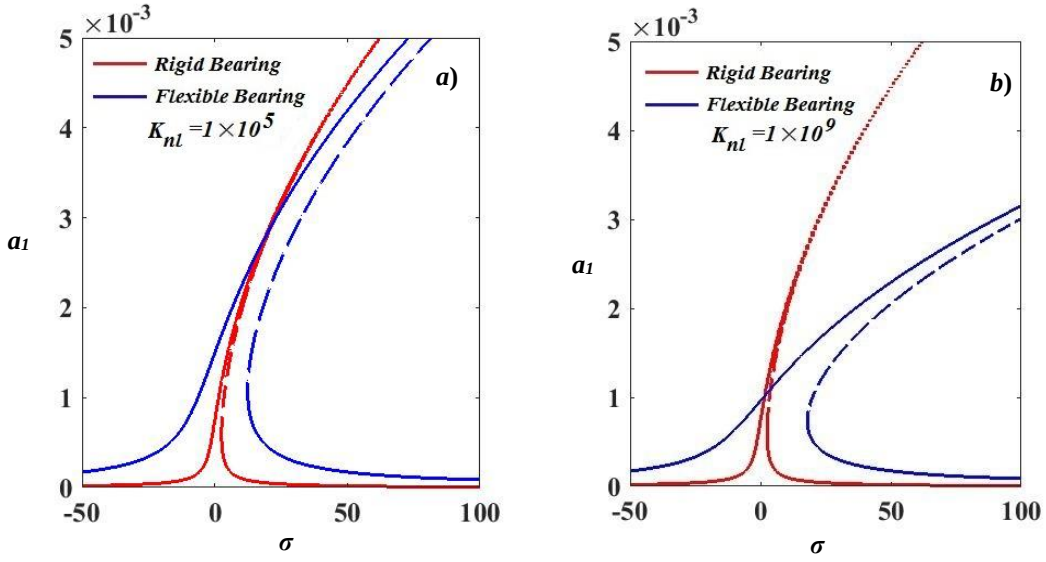

Fig.3.26: Frequency response plots if $\Omega_1 \approx 2\omega_1$ and $\Omega_2 \approx \omega_1$: P_0=1×10³N, P_1=5×10³N, K_l=1×10⁵N/m.

The influence of the flexible bearings has been shown to Fig.3.26 and it has been noted that the vibration amplitude is found to be minimum when the rotor-disk is supported on the flexible bearings. The nonlinearity of the support bearings leads to a hardening effect and an appreciable effect in the amplitude reduction (corresponding to particular σ) can be observed along with a hardening effect in the curve for the system with the nonlinear stiffness K_{nl} =1×10⁹ N/m^3. Hence, the flexible bearings offer more stable with minimum vibration amplitude than the rigid support for considered configuration.

a. ***Resonance Condition:*** $\Omega_1 \approx 2\omega_1$

Figures 3.27-3.32 depict the frequency response characteristics for the resonance condition when Ω_1 is nearly equal to the $2\omega_1$ against change in the design parameters such as disk radius, disk location, spin speed, linear and nonlinear stiffness of the bearing support, a static and a pulsating axial load.

Apart, the frequency response curves exhibit hardening effect and as a result, the vibration amplitude is mostly observed to be decreased with an increase in the any control parameter. In fact, whether the vibration amplitude gets increased or decreased or remained the same is depending upon the interacting influences of the design parameters. Figure 3.27 illustrates the influences of changing a radius of the shaft on the system stability and bifurcation. It has been observed that an increase in the vibration amplitude is experienced with an increase in radius of the disk as the curve shifts toward the left side and losses the hardening effect. Hence, the system experiences softening behavior from the hardening state. The reason might be that with increase the radius, the inertia forces increase over the restoring forces. The trivial state instability region i.e., unstable trivial solution (between supercritical and subcritical pitchfork bifurcation) gets increased with an increase in radius of the disk. Consequently, we can say that the dynamic behavior of the system can prominently be affected due to the change in the radius with an increase in the instability region. Moreover, the possibility of catastrophic failure as a sudden change in the amplitude due to jump up i.e., from the unstable trivial solution to the non-trivial solution gets high with an increase in the radius.

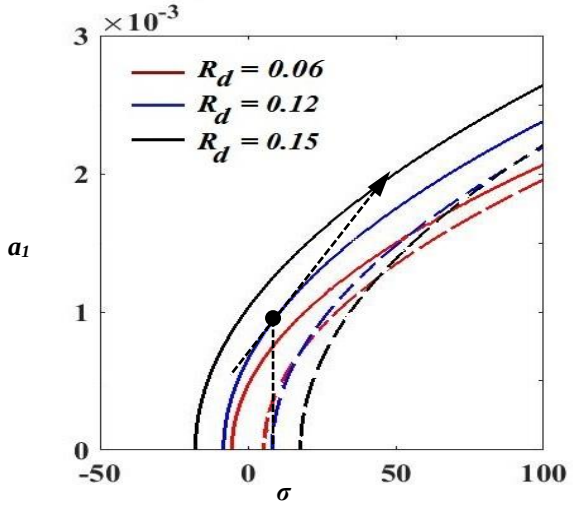

Fig.3.27: Frequency response plot if $\Omega_1 \approx 2\omega_1$: $P_0=1\times10^3N$, $P_1=5\times10^3N$

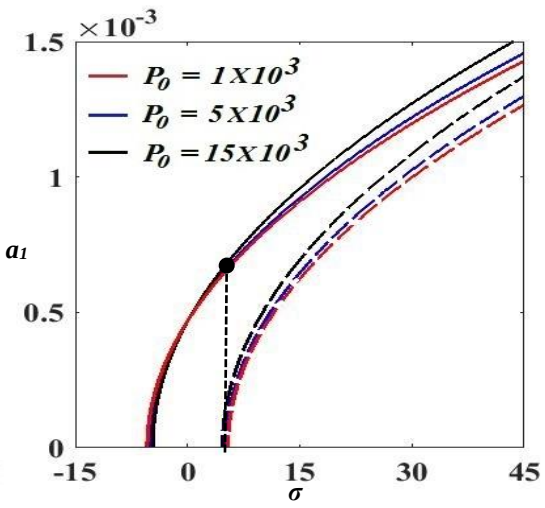

Fig.3.28: Frequency response plot if $\Omega_1 \approx 2\omega_1$: $P_1=5\times10^3N$

Figure 3.28 depicts the overall vibration characteristics with increase in a magnitude of the static force P_0 but this change is slightly smaller near σ = 0 i.e., exactly at the resonance condition. A region of the instability due to the trivial solution remains unchanged with increase in the axial force while a slight change in the vibration amplitude appears with increase in the axial force. Hence, the static component of the pulsating force does not influence the overall dynamics of the system. The change in spin speed (Ω_2) has no influence on the hardening effect depicted in Fig.3.29. While distinguishable change can be detected in the instability region. An increase in the spin speed causes the system more dynamically stable as the breadth between the curve lines and shifting of the critical point to lower frequency.

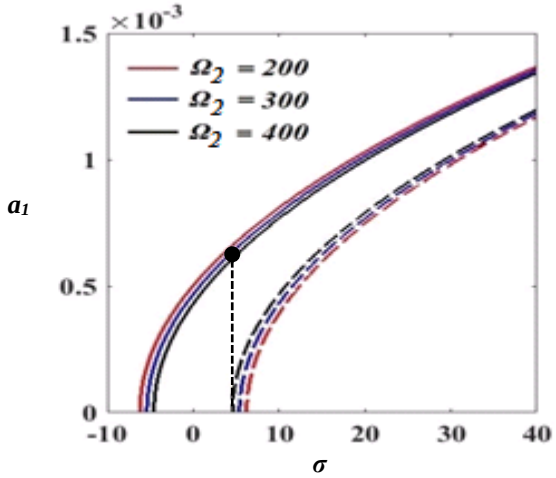

Fig.3.29: Frequency response plot if $\Omega_1 \approx 2\omega_1$: $P_0=1\times10^3N$, $P_1=5.0\times10^3N$

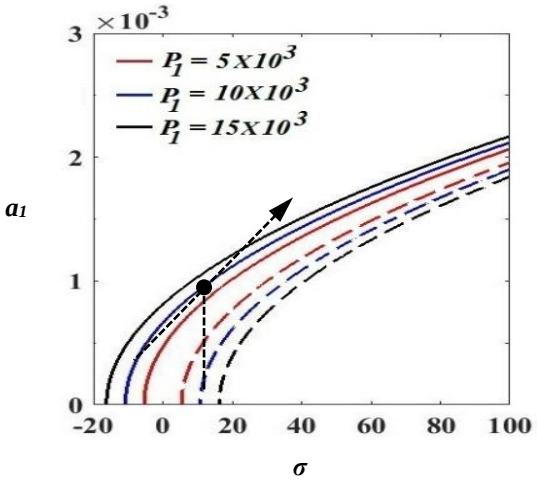

Fig.3.30: Frequency response plot if $\Omega_1 \approx 2\omega_1$: $P_0=1\times10^3$

We observe in Fig.3.30 that the rise in a magnitude of the pulsating force P_1 results in an increase in the vibration amplitude along with the trivial state instability to that of higher value. Further, the jump length increases with increase in the dynamic force component. A noticeable effect in the hardening characteristic of the system due to a change in the disk location can be observed in Fig.3.29. The curve bents more toward the right side when the disk is mounted at a point away from the mid span of the shaft. Thus, the system experiences more hardening effect that leads to decrease in the vibration amplitude with the relocation the disk from the mid-point. However, the expansion of the curve with the disk location $l/3$ is more than the other cases. Consequently, it significantly affects the dynamic behavior of the rotating system. Interestingly,

the region where the trivial solution losses the stability gets rises, when the amplitude of the pulsating force gets increased.

Figures 3.32-3.33 present the effect of linear and nonlinear stiffness coefficients of the flexible bearings on the frequency characteristics. With an increase in both the linear and nonlinear stiffness, the vibration amplitude decreases remarkably as the restoring force becomes more dominant over the externally influenced forces. Hence, uses of the flexible bearings are considered to be substantially safe in the working condition since it reduces the chances of failure due to a negligible jump length. As well as, it has been observed that an increase in the nonlinear component over the linear system causes the system to be more secure and stable. Hence, the nonlinear stiffness component offers more stable than its linear counterpart. However, the range of instability i.e., remains unchanged with increase in these values.

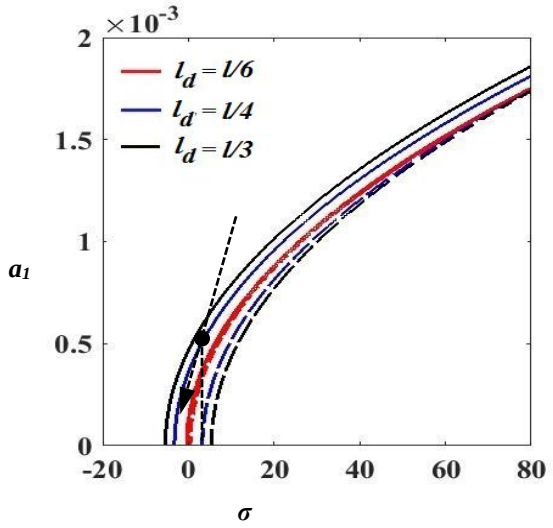

Fig.3.31: Frequency response plot if $\Omega_1 \approx 2\omega_1$: $P_1=1\times10^3N$, $P_0=5\times10^3N$

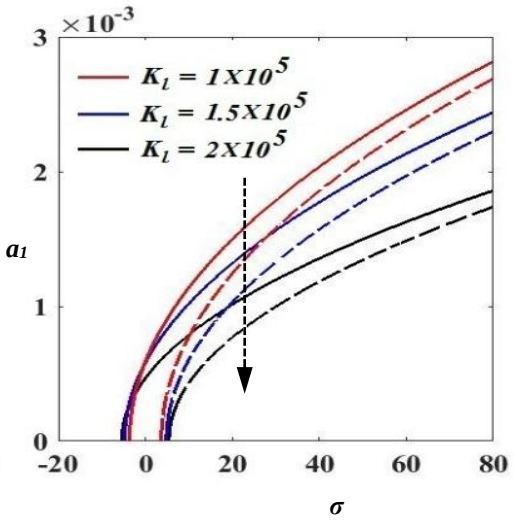

Fig.3.32: Frequency response plot if $\Omega_1 \approx 2\omega_1$: $P_1=1\times10^3N$, $P_0=5\times10^3N$

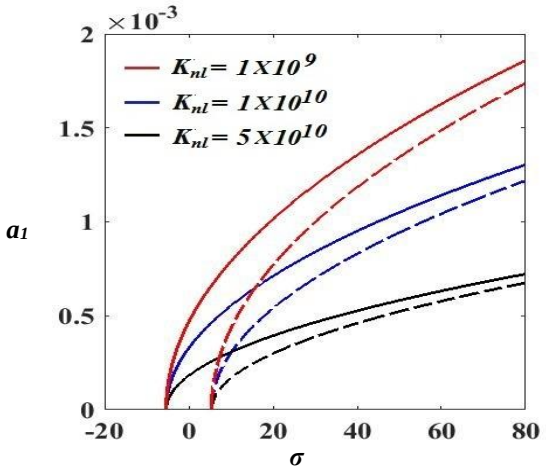

Fig.3.33: Frequency response plot if Ω1≈2ω1: $P1=1\times10^3N$, $P0=5\times10^3N$

b. ***Combination Resonance Condition:*** $\Omega_1 \approx 2\omega_1$ ***and*** $\Omega_2 \approx \omega_1$

Figures 3.34-3.39 describe frequency response characteristics of the system considering the combined resonance condition when the frequencies of the pulsating force and the mass unbalance are closely matched with $2\omega_1$ and ω_1, respectively to demonstrate the safe zone of an operating condition. Subsequent catastrophic situations when the change in the different

parameters such as disk radius, disk location, spin speed, static and pulsating axial load lead to unwanted circumstances.

The influence of radius of the shaft onto the system dynamics and inherit vulnerability situation have been depicted in Fig. 3.34. With increase in the shaft radius while the response amplitude becomes unaltered, the bifurcation starts at a lower frequency and thus the nonlinear behavior of the system can be affected prominently by the radius.

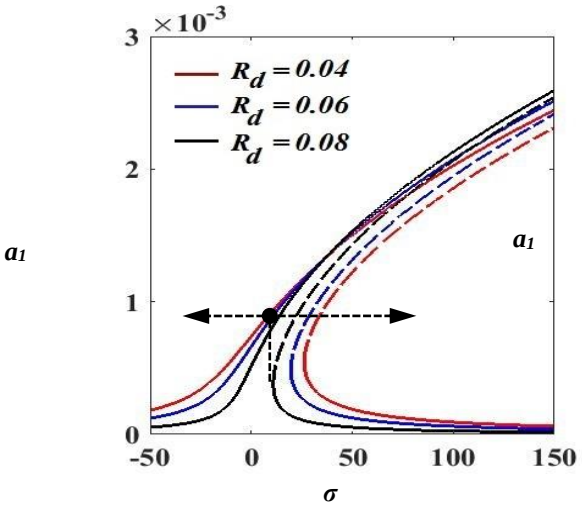

Fig. 3.34: Frequency response plot if $\Omega_1 \approx 2\omega_1$ and $\Omega_2 \approx \omega_1$: $P_0=1\times10^3$ N, $P_1=1\times10^3 N$

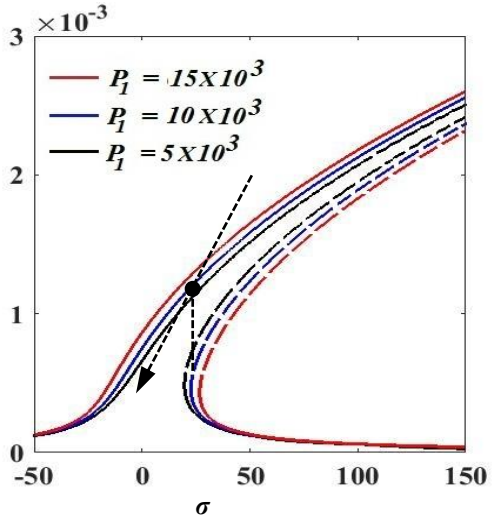

Fig. 3.35: Frequency response plot if $\Omega_1 \approx 2\omega_1$ and $\Omega_2 \approx \omega_1$: $P_0=1\times10^3 N$

With increase in the shaft radius, there is a shift in the bifurcation point toward the right and as a result, a safe operating range gets higher. It has been observed that with an increase in the amplitude of the pulsating axial force, both the response amplitude and the position of the bifurcation get influenced while the vibration amplitude increases with an increase in the axial force as shown in Fig. 3.35. In addition, the forward change in amplitude of the axial force offers a benefit to the operating condition since it introduces the bifurcation at a higher frequency. Thus, the system loses its stability at the higher working frequency.

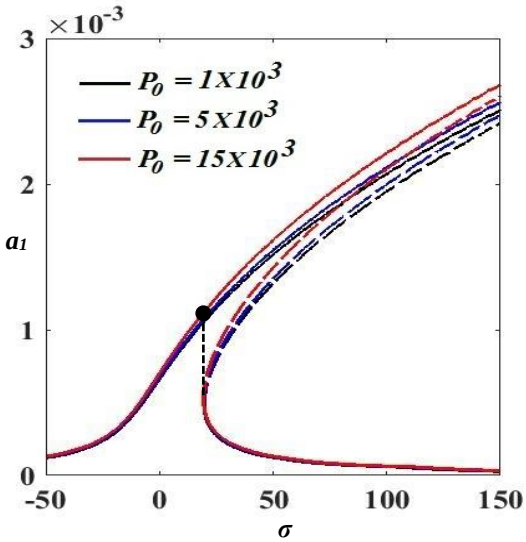

Fig. 3.36: Frequency response plot if $\Omega_1 \approx 2\omega_1$ and $\Omega_2 \approx \omega_1$: $P_1=5\times10^3 N$

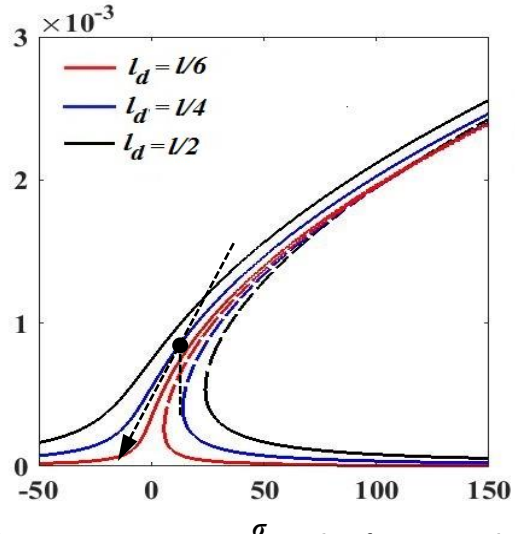

Fig.3.37: Frequency response plot if $\Omega_1 \approx 2\omega_1$ and $\Omega_2 \approx \omega_1$: $P_0=1\times10^3$ N, $P_1=5\times10^3$ N

However, with increase in a static component of the axial force, there is an insignificant influence onto the bifurcation as shown in Fig. 3.36. The influences of disk location away from the mid-span have been indicated in Fig.3.37. The system is found to be stable for a wide range of the unbalance frequency without experiencing any jump phenomena when the disk location is exactly at the mid-point. This might be due to canceling out the gyroscopic and Coriolis effect. However, a region with single stable solution found to be exist when the disk location is at *l/2* as shown in Fig.3.37.

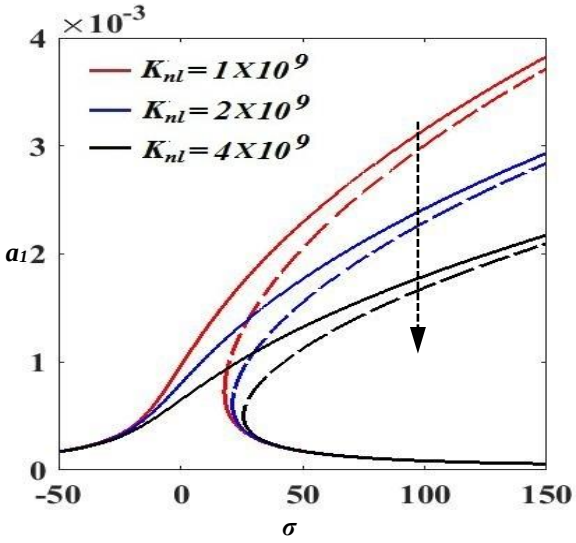

Fig.3.38: *Frequency response plot if* $\Omega_1 \approx 2\omega_1$ *and* $\Omega_2 \approx \omega_1$*:* $P_0 = 1\times10^3$ *N,* $K_{nl} = 1\times10^9$ *N/m*

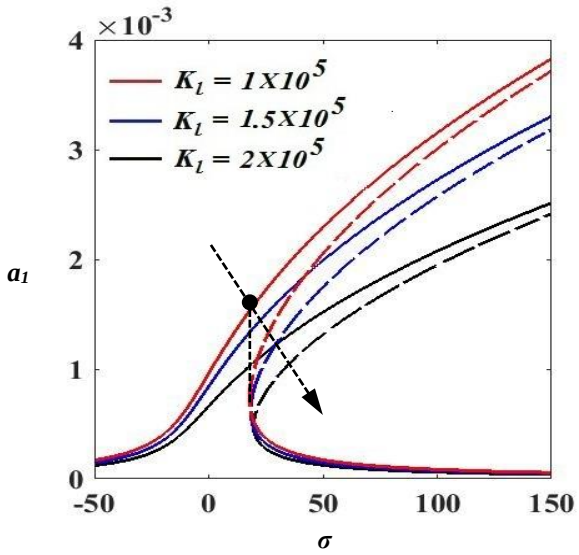

Fig. 3.39: Frequency response plot if $\Omega_1 \approx 2\omega_1$ and $\Omega_2 \approx \omega_1$: $P_0 = 1\times10^3$N, $K_l = 1\times10^5$N/m

Figures 3.38-3.39 present the influences of the linear and nonlinear stiffness of the supporting bearings for obtaining the bifurcation point with an increase in both the linear and nonlinear stiffness coefficient. The vibration amplitude and the jump length decrease with an increase in the value of any these two spring components as the restoring force becomes more dominant over the externally influenced forces. Similar to the case of the primary principle resonance condition, here also the nonlinear stiffness component offers more stable than the linear counterpart. The system is found to be more stable when we increase K_{nl} instead K_l.

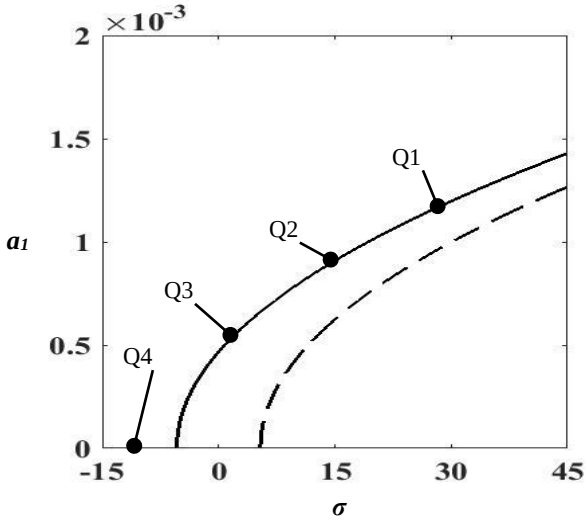

Fig. 3.40: Frequency response plot **:** $\Omega_1 \approx 2\omega_1$

Figures 3.40 - 3.41 are demonstrated to depict an accuracy of the obtained results using the perturbtion technique with respect to the results obtained by numerically solving the equations of motion. Here, a detuning parameter σ has been taken as 30, 15, 1, and -12 respectively for resonance condition $\Omega_1 \approx 2\omega_1$. Figure 3.40 portrays the frequency response which

has been verified at point *Q*1, *Q*2, *Q*3 and *Q*4 by comparing with the time histories, FFT and Poincare's map of Fig.3.41, respectively. The results using the both schemes are found in a compliance.

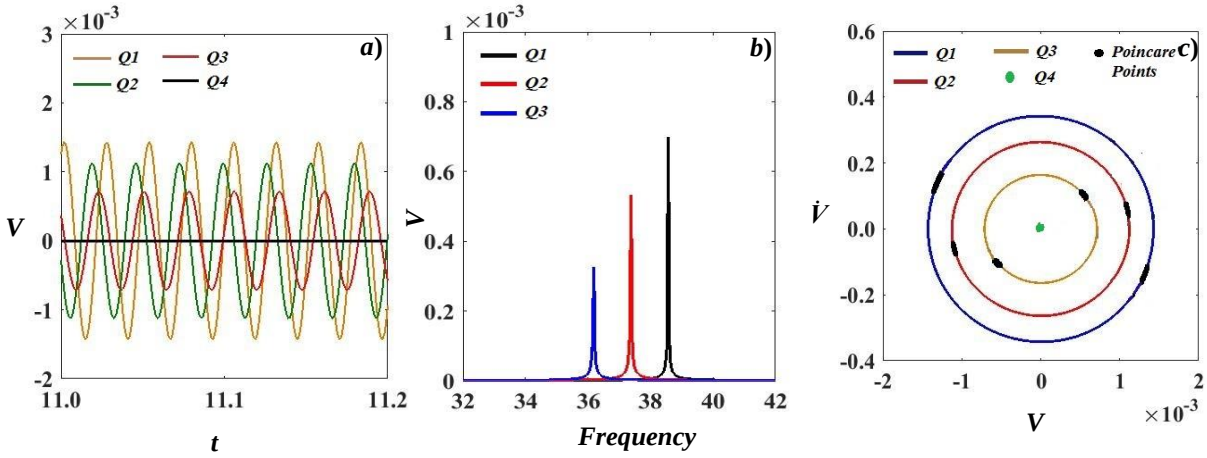

Fig. 3.41: Steady state response only (Ref.3.40) a) Time response b) FFT plot c) Phase portrait and Poincare map

In Fig. 3.41, a periodic motion is observed in the time history and corresponding FFT shows a peak at a half frequency than that of the excitation. Closed circular/elliptic type trajectories can be observed on the phase space trajectories that denote periodic behavior of the system along with the dominance of the single frequency (i.e Ω_2). The two points on the Poincare's maps depict double periodic behavior of the system. Figure 3.41 shows a decrease in the amplitude of the system near the point *Q*4 (Fig.3.40) and eventually it reaches zero due to the existence of atrivial solution. This is due to vibrations of the system at the two frequencies which can be detected in the corresponding Fast Fourier transform. The presence of two frequencies causes torus type trajectories in the phase plane plots. The Poincare's maps corresponding to the phase space have shown closed curve, it indicate the system has quasiperiodic behavior at these points. At point *Q*4, the system came to a trivial solution because it showed attraction toward equallibra after a few oscillations.

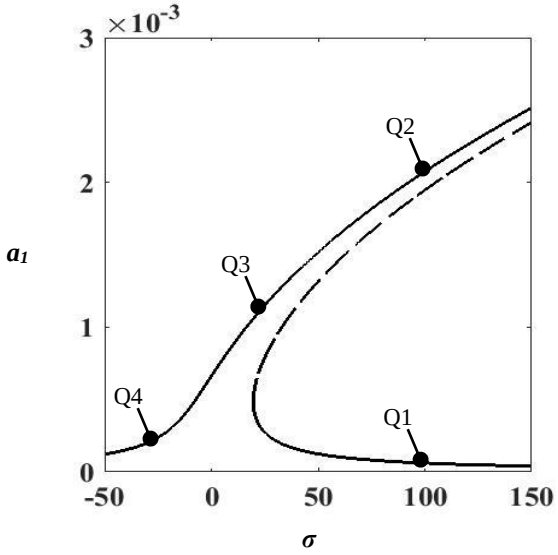

Fig.3.42: Frequency response plot : $\Omega_1 \approx 2\omega_1$ *and* $\Omega_2 \approx \omega_1$

Figure 3.42 portrays a frequency response curve which has been verified at points *Q*1, *Q*2, *Q*3 and *Q*4 by comparing with the time responses of 3.43, respectively. Here, a combined resonance condition $\Omega_1 \approx 2\omega_1$ with $\Omega_2 \approx \omega_1$ is considered. Figure 3.43 is portrayed by numerically solving the equations of motion for detuning parameters σ = 100, 20 and -30. Points *Q*1 and *Q*2

denote a lower and higher limit cycle at σ = 100, respectively. Time integration of the equations of motion with initial condition $V(0)$ = 0.005 is performed and the system shows behavior corresponding to point $Q1$ at σ = 100 for a steady state. With similar configuration of the system, Initial condition $V(0)$ = 0.012 results in a steady state behavior of the system which is corresponding to Point $Q2$. The FFT plot shows a peak, so the excitations (i.e an unbalance and a periodical axial load) have influence on the system behavior at point $Q1$ but with a dominance of the unbalance excitation. As both excitation frequencies are incommensurate, the corresponding Poincare's map shows quasiperiodic behavior.

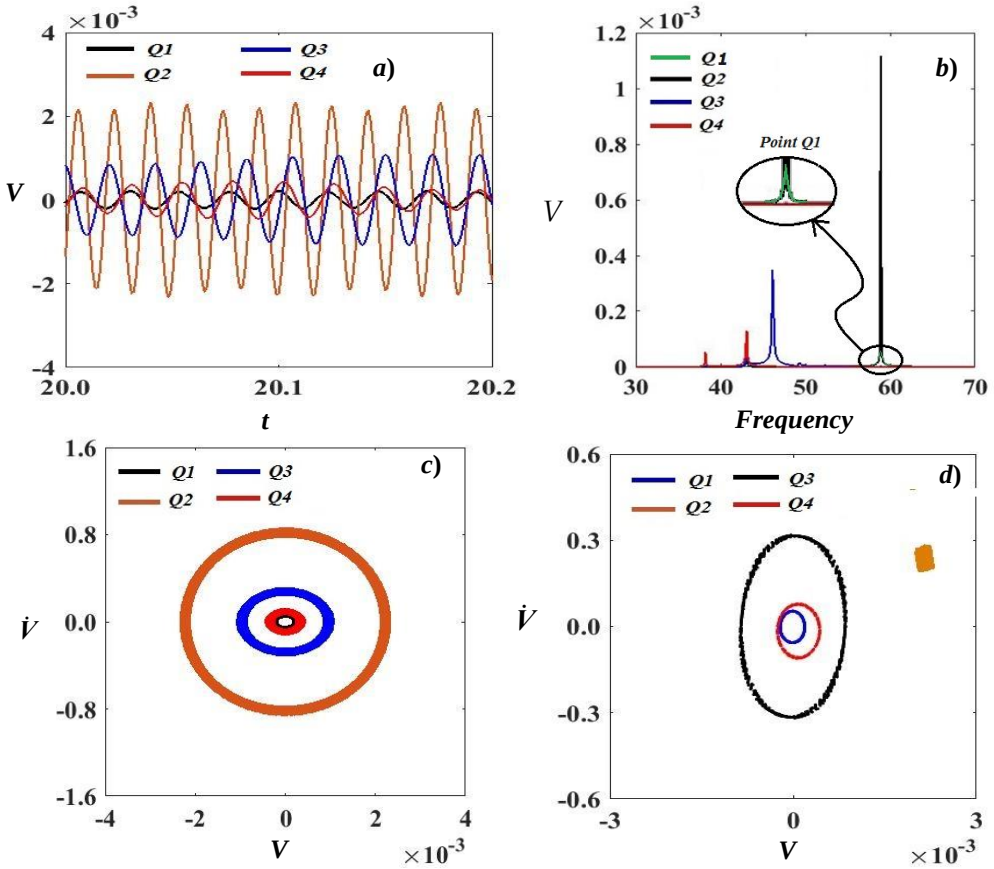

Fig.3.43: Steady state response only (Ref.Fig. 3.42) a) Time response b) FFT plot c) Phase portrait d) Poincare map

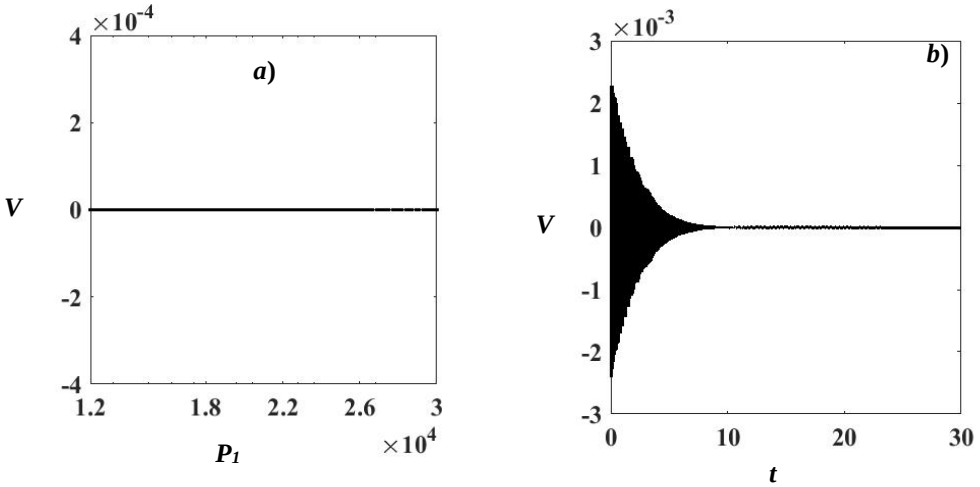

Fig.3.44: a) Bifurcation diagram of P_1 **b)** Time response plot: $\Omega_1 = 0.8\omega_1$, P_0= 5000 N, K_l=2×10^5 N, K_{nl} =3×10^9N/m^3

In FFT of Q2, a single peak and a single point on the Poincare's map also can be observed, So it can be depicted that the rotating system has a periodic behavior near point $Q2$ with a sole dominance of the unbalance excitation. The Poincare's map corresponding to points Q3 and Q4

show quasiperiodic behavior of the system near points $Q3$ and $Q4$. As well as, the FFT of Q4 shows clear two peaks. Thus the system has more influence of the pulsating axial force at point $Q4$ than at point $Q3$. Hence, it can be depicted that the system undergoes a periodic/quasiperiodic behavior. Therefore, the initial condition plays important role in determining type of the system behavior (i.e point Q1 or point Q2) in the instability region.

Figure 3.44a portrays system behavior with P_1 as a control parameter when $\Omega_1 = 0.8\omega_1$ with initial condition $v(0) = 0.002$, it shows trivial solutions for above range of P_1.The same can be depicted from Fig. 3.44b which is obtained at $P_1 = 1.5\times10^4 N$,so the system does not shows the effect of a change in P_1. 3.45 shows a sudden double periodic nature of the system near P_1=1.4×10⁴ N, but it does not last long with an increase in P_1 value when Ω_1=2.3ω_1. It shows again a trivial solution after 1.9×10⁴N. Figure 3.46a shows a steady state in the time series with dominance of only one frequency which is a half of the excitation frequency value for Ω_1=2.3ω_1. The correspoding Poincare' clearly shows a double periodic motion of the system at $P_1 = 1.6\times10^4 N$.

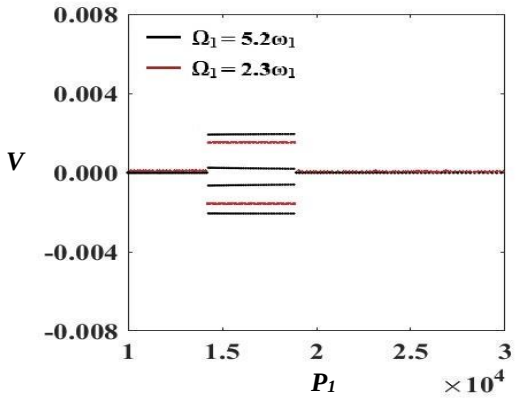

Fig.3.45: Bifurcation diagram of P_1, P_0=5000 N, K_l=2×10⁵ N, K_{nl}=3×10⁹N/m³

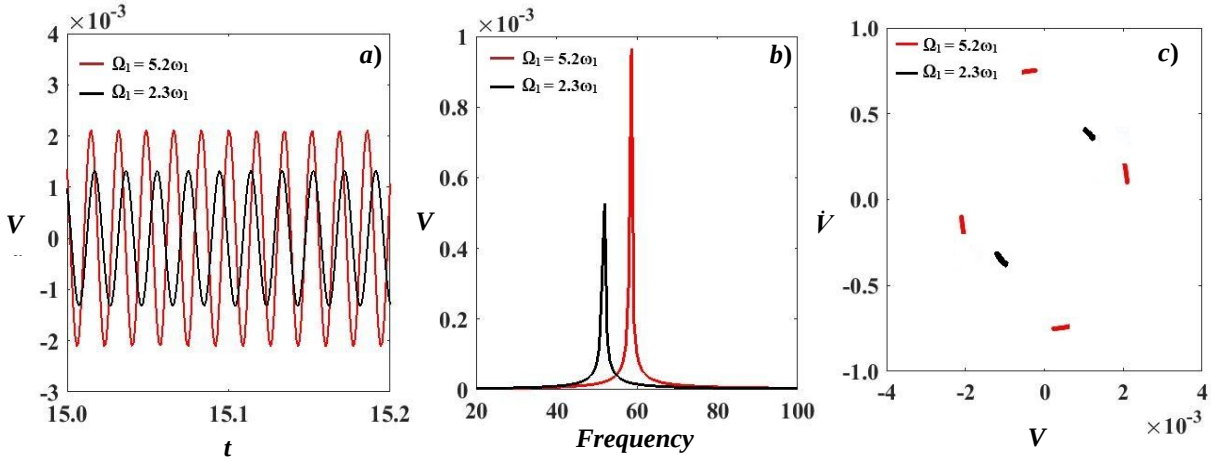

Fig.3.46: Steady state response only a) Time response b) FFT plot c) Poincare map: P_1 = 15000 N, P_0=5000 N, K_l=2×10⁵ N, K_{nl} =3×10⁹ N/m³

Figure 3.45 shows the system behavior with four periods near P_1 =1.5×10⁴N when Ω_1=2.3ω_1, but it does not last long with an increase in P_1 value. The amplitude of P_1 is found critical between 1.5×10⁴ N - 1.9×10⁴N thus it is advisable to avoid the range of P_1 between 1.5×10⁴ N - 1.9×10⁴N in order to ensure a safe and smooth operation. It shows again trivial solution after 1.9×10⁴N. Figure 3.46a shows a steady state in the time series with a dominance of only one frequency which is 1/4th of the excitation frequency. The corresponding the Poincare's map clearly shows the motion of the system with four period at $P_1 = 1.6\times10^4 N$.

c. *Validation of the present model with the published research*

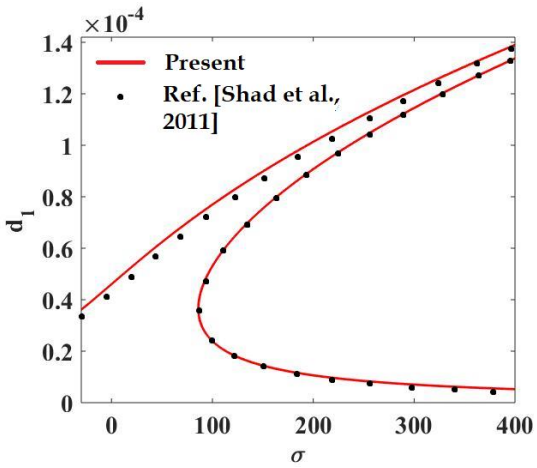

Fig.3.47 : Validation-Frequency response plot

For purpose of validation of the proposed model, the frequency response plot (Fig.3.47) is portrayed by neglecting the flexible bearing effect and the base excitation with considering the same configuration as Shad et al. (2011). The solid red colour lines represent results from the proposed model and the black dotted lines represent results from a published article by Shad et al. (2011). It has been found that the results of proposed models are in concurrence with the those presented by Shad et al. (2011).

3.5 Summary

Numerical investigation of the rotor-bearing system having considering the structural nonlinearity due to higher order deformation in bending has been carried out. The nonlinear mathematical model has been developed incorporating the mid-plain stretching phenomenon in the shaft element in addition secondary effects like rotary inertia effects, gyroscopic effects, rotor mass unbalance, base motion and axial loading. The method of multiple scales is used to solve this model including the nonlinear terms. This method is applied directly to the partial differential equation of motion and to the discretized equations. While Campbell diagrams as a part of free vibration have been illustrated under the variation of physical parameters of the system, an evidences of chaotic response i.e., route to chaos upon changing the control parameters have been investigated by depicting of time history, Fourier spectrum and Poincare's section. The frequency response curves have been plotted for the resonance conditions under the influences of various control parameters. Stability and critical points have been analysed for a wide range of the various system parameters.

The effect of nonlinearities and other variations for the different parameters like amplitude of excitation, mass unbalance, position of disk, and mass of the disk on the system performance has been performed. Bifurcations and stability of the obtained solution have been studied.

Here, we considered the disk parameters and disturbance parameters (i.e., base excitation, axial force and mass unbalance) as design parameters and their influences on dynamic behavior of the proposed rotating system.

With increase in the disk parameters can reduce the hardening effect and helps to shift instability region to a high frequency. As a result, bifurcation starts at a higher frequency and leads to a stable operating range until the operating frequency reaches to one of the critical natural frequencies of the system. Here, the system loses its stability due to the saddle-node and pitchfork bifurcation, respectively with the sudden jump phenomena.

The base excitation plays an important role in deciding the vibration behavior of the system. It has been observed that the variation in the values of the excitation parameters causes the system to experience a transformation of its behavior from the quasi-periodic to the chaotic nature.

The proposed model, the pulsating axial load along with the mass unbalance shows appreciable effect on the dynamic behavior of the system such as an increase in these positive effect causes rise in an amplitude of the system vibration. Increasing the static axial load has been ensured the stability of the system since it increases the natural frequency of the whole system. The possibility of a catastrophic failure as a sudden change in the amplitude due to the jump up i.e., from the unstable trivial solution to the non-trivial solution gets high with increase in the disk-size with radius.

The flexible bearings are considered to substantially safe in the working condition since it reduces chances of failure due to the jump length. The vibration amplitude and jump length decreases with increase in the value of any these linear and nonlinear spring components. From these critical observations, we can conclude with the evidences that monitor and control the vibration characteristic and its behavior to avoid catastrophic failure can be successfully controlled with the adjustment of the design parameters. It helps further to design the system which can run in its operational speed range satisfactorily.